

Drone-based photogrammetry combined with deep-learning to estimate hail size distributions and melting of hail on the ground

Martin Lainer¹, Killian P. Brennan^{1,a}, Alessandro Hering¹, Jérôme Kopp², Samuel Monhart¹, Daniel Wolfensberger¹, and Urs Germann¹

¹Federal Office of Meteorology and Climatology, MeteoSwiss, Locarno-Monti, Switzerland

^anow at: Institute for Atmospheric and Climate Science, ETH Zurich, Zurich, 8092, Switzerland

²Oeschger Centre for Climate Change Research and Institute of Geography, University of Bern, Switzerland

Correspondence: Martin Lainer (martin.lainer@meteoswiss.ch)

Abstract. Hail is a major threat associated with severe thunderstorms and ~~an estimation of~~ estimating the hail size is important for issuing warnings to the public. ~~Operational radar products exist that estimate the size of the expected hail. For the verification of such products, ground-based~~ For the validation of existing, operational, radar-derived hail estimates, ground-based observations are necessary. Automatic hail sensors, as for example within the Swiss hail network, record the kinetic energy of hailstones ~~and can estimate with this the hail diameters. However, due to~~ estimate the hail sizes. Due to the small size of the observational area of these sensors (0.2 m^2) ~~the estimation of the~~, the full hail size distribution (HSD) ~~can have large uncertainties. To overcome~~ cannot be retrieved. To address this issue, we ~~combine drone-based aerial photogrammetry with~~ apply a state-of-the-art custom trained deep-learning object detection model to ~~identify hailstones in the images~~ drone-based aerial photogrammetric data to identify hailstones and estimate the HSD ~~in a final step. This approach is applied to photogrammetric~~ image. Photogrammetric data of hail on the ground ~~from a supercell storm, that crossed~~ was collected for one supercell thunderstorm crossing central Switzerland from southwest to northeast in the afternoon of June 20, June 2021. The hail swath of this intense right-moving supercell was intercepted a few minutes after the passage at a soccer field near Entlebuch (Canton Lucerne, Switzerland) and aerial images ~~of the hail on the ground~~ were taken by a commercial DJI drone, equipped with a ~~50 megapixels~~ 45 megapixel full frame camera system. The ~~average resulting images have a~~ ground sampling distance (GSD) ~~that could be reached was of~~ 1.5 mm per pixel, which is set by the mounted camera objective with a defined by the focal length of 35 mm of the camera and a flight altitude of 12 m above ground. A 2D orthomosaic model of the survey area (750 m^2) is created based on 116 captured images during the first drone mapping flight. Hail is then detected by using a region-based Convolutional Neural Network (Mask R-CNN). We first characterize the hail sizes based on the individual hail segmentation masks resulting from the model detections and investigate the performance by using manual hail annotations by experts to generate validation and test data sets. The final HSD, composed of 18209 hailstones, is compared with nearby automatic hail sensor observations, the operational weather radar based hail product MESHS (Maximum Expected Severe Hail Size) and ~~some~~ crowdsourced hail reports. Based on the retrieved ~~drone hail~~ data set, a statistical assessment of sampling errors of hail sensors is carried out. Furthermore, five repetitions of the drone-based photogrammetry mission within ~~about 18~~ 18.65 min ~~give the unique opportunity to investigate~~ facilitate investigations into the hail melting process on the ground ~~for this specific~~ supercell hailstorm and location.

1 Introduction

Hail is a severe ~~danger hazard~~ associated with thunderstorms and ~~its impact increases with its~~ the threat and potential damage increases with increasing hail size. Therefore, the estimation of the hail size is important ~~for an appropriate warning of to issue appropriate warnings to~~ the public and to ~~asses assess~~ the damage. ~~The hailstorms in the period between~~ Between 18 June and 30 31 July 2021 ~~were extremely intense a period of intense hail storms occurred~~ over Switzerland (Kopp et al., 2022). ~~According to la Mobilière (2021), the amount of storm-related losses in Switzerland accumulated to around~~ 340 million (CHF) ~~storm-related losses are estimated~~ in the month of June ~~alone~~ and large hail played a significant role (la Mobilière, 2021). Operational weather radar-based algorithms ~~exist, which try to compute~~ allow for the computation of the the maximum expected severe hail size (MESHS, Treloar, 1998) and probability of hail (PoH, Waldvogel et al., 1979) within a thunderstorm. In Switzerland, those 35 products are derived from five C-band weather radars operating in the complex terrain of the ~~alps~~ Alps (Germann et al., 2022) and have a spatial resolution of 1 km². ~~For~~ Ground-based observations are crucial for the verification and improvements of ~~such~~ radar-based hail products, ~~ground-based observations are needed~~.

~~Beside~~ Besides traditional hailpads, which are cost effective ~~and but~~ do not provide any ~~time information, promising other observational approaches and tools include newly developed~~ temporal information, new automatic hail sensors (Löffler-Mang 40 et al., 2011) and crowdsourced hail reports (Barras et al., 2019). ~~Recently,~~ provide valuable additional hail observations. Within the framework of the Swiss Hail Network project (Romppainen-Martius, 2022; Kopp et al., 2022) a network of 80 automatic hail sensors was installed in ~~the three most~~ three hail-prone regions ~~of in~~ Switzerland (Jura, southern Ticino and Napf) ~~according to climatology studies (Nisi et al., 2018, 2016) in the framework of «The Swiss Hail Network» project (Romppainen-Martius, 2022; Kopp et al., 2022) that are identified as hail hot spots based on climatological studies (Nisi et al., 2018, 2016)~~ 45 . These sensors ~~record the kinetic energy of single hailstones and infer their sizes with a precise time information, but provide no shape (axis ratio) information and have only a small impact~~ provide an estimate of the hail size and the exact time of the impact, but no information about the shape. In addition, hail sensors cannot capture the entire hail size distribution (HSD) due to their small observational area of 0.2 m². ~~The crowdsourced hail data usually only gives information about the largest observed hail diameters. The quality control of crowdsourced hail observations is difficult and the data has a low accuracy due to predefined fixed size categories (smaller than coffee bean: > 0–5 (Kopp et al., 2023). Similarly, crowdsourced hail reports use predefined categories (no hail, < 10 mm, coffee bean: 5–8 10 mm, 1 CHF coin: 23 20 mm, 5 CHF coin: 32 30 mm, golf ball: 43 50 mm , tennis ball: 68 and > 70 mm) . Another source of uncertainty arises from the size estimates submitted by the app users for estimating the hail size, corresponding to an unknown percentile of the actual HSD. Besides that, their quality control is challenging~~ (Barras et al., 2019).

55 ~~Hail sensors cannot capture the entire hail size distribution (HSD) of a hail storm due to their limited area (Kopp et al., 2023)~~ In order to overcome some of the limitations of automatic hail sensors and crowdsourced reports only give information about the largest hailstone, therefore they cannot be used to infer a complete HSD. A for estimating the HSD, a new technique, called HailPixel, has been introduced by Soderholm et al. (2020) for measuring the size distribution of hail. They propose to use aerial imagery captured by an unmanned aerial vehicle (UAV) to survey hail on the ground over a large ~~detection area using aerial~~

60 imagery captured from a small unmanned aircraft and area. The resulting image data is analyzed using deep-learning techniques combined with computer vision feature extraction. They show exemplary to estimate the HSD. The results from a *HailPixel* survey of a hailstorm in San Rafael (Argentina) in the context of existing studies and point out potential improvements for future hail surveys. With a sample of clearly demonstrates the advantage of this technique, as an UAV can survey an extended area and capture a large sample of hailstones. They identified 15983 measured hailstone sizes, they were able to precisely define the shape and tails of the HSD. hailstones which allows to infer the HSD of the event.

A main advantage of image-based hail data sets over crowdsourced, hail sensor and hailpad data is, that the larger detection area allows to derive a more complete HSD. Likewise with hailpads, the shape factor in the image plane can be easily determined as well. It is known, that hailstones usually have an oblate spheroid shape with mean axis ratios close to 0.8, though they can sometimes have large protuberances (Knight, 1986). In this study, we present detailed statistics of the observed hail aspect ratios for a particular hail event and location.

65 On we use aerial drone images collected on 20 June 2021. That day, the ingredients for long-living and well-organized severe thunderstorms came together over (humid air, high instability and strong wind shear) were in place across Switzerland. An air mass with steep lapse rates was advected from the southwest was advected on top of decent, above a moist low-level moisture. As the air with mean mixing ratios around 12 sounding from the meteorological station Payerne in Fig. 1 points out, during the course of the day SB (g kg^{-1} , Lapse rates above the capping inversion were close to dry adiabatic. The Surface-Based) CAPE (Convective Available Potential Energy) values of more than (SBCAPE) was above 2000 J kg^{-1} developed in conjunction with a high 0–6 and high wind shear of about 30 m s^{-1} . A hail-producing strong supercell was chased on that day. The temporal track of this supercell from radar data in the layer 0–6 km was present at 12 UTC (Fig. 1). A supercell developed over the French Alps in the morning and moved through Switzerland within 5 hours. The track of the supercell is shown in Fig. 2(a). At 12, when the radio sounding took place, the cell was located above the French alps (magenta circle). It entered Switzerland 30 later and crossed the country in a period of 5 hours (s. storm track and was generated based on the TRT (Thunderstorm Radar Tracking) algorithm (Feldmann et al., 2023; Hering et al., 2004). From the hodograph shown in Fig. 2(a) A deeper analysis of the storm motion and 1 a storm motion vector of 234° at 13 m s^{-1} (according to Bunkers et al. (2000)) and mean storm relative winds based on the hodograph display (s. (0–6 Fig. km) of 71° at 9 1), shows that the m s^{-1} can be derived. This environment favored the development of classical right-moving supercells (Houze et al., 1993) on that day.

85 Based on the MESHS products from the Swiss C-band radar network (Germann et al., 2022), we find that the hail swath was nearly uninterrupted from the north-eastern edge of The supercell produced a continuous hail swath from lake Geneva to the north-western edge of lake Zurich over a length of about 155 km. The maximal width of and the maximum hail size is estimated above 60 mm. Both, the maximum hail size and the hail swath part exceeding a MESHS value of 6 was in the order of 10 are inferred from the MESHS products based on the Swiss operational radar network (Germann et al., 2022). Figure 2(b) illustrates the radar derived MESHS signature from the supercell when it crossed central Switzerland, just a little south of in the Napf region (predominantly rural area), where a cluster of automatic hail sensors are installed. MESHS reached 6.3 when the hail from the supercell was intercepted at central Switzerland) where the aerial images were collected on a soccer field (magenta white cross) near Entlebuch (Canton Lucerne). The same MESHS values were present at the two closest hail sensor locations

95 ~~(HS1 and HS2 on map in Fig. 2(e) and (d)). For this location MESHs indicates a maximum expected severe hail size of 63 mm and (d)).~~
~~At the two other sensor locations (HS3 and HS4) MESHs reached lower values of 48 mm and on-site observations revealed~~
~~maximum dimensions between 40 mm and 58 mm (Fig. 2(e)). In addition, data from four automatic hail sensors are available~~
~~for the area within a distance of less than 1 km (d)). Interestingly, the very close sensor HS1 (300 m SSW from the soccer field) did not~~
100 ~~get record any impact during the passage of the hail core. Because of~~
~~the absence of any record on this closest sensor entire hail event. Therefore,~~ we use the hail data from the other remaining 3
sensors, which are in the vicinity of the drone hail survey area. As a note, in this analyses, HS2 and HS4 are located NNE of
the soccer field at a distance of 770 m, respectively and 1470 m, to the NNE direction of the soccer field respectively, while
HS3 is located SSW at a distance of 1150 m to the SSW (Fig. 2(e)3).

Soderholm et al. (2020) provided recommendations for drone-based hail surveys in general: Ideally conduct them on general
105 recommendations to optimize the quality and further analysis of aerial drone images of hail: uniform and contrasting back-
grounds (cut or grazed turf grasses); Increase the high camera resolution for capturing smaller hailstones; Minimize minimize
the melting of hailstones and; avoid aerial surveys in areas with flowing water and conduct surveys as immediately as possible
immediately after hail fall stops to prevent further melting. Following those suggestion, we have put effort in using suggestions,
we used a camera equipment that allows to take pictures in a higher resolution to increase the has a high resolution giving a
110 ground sampling distance (GSD) to of 1.5 mm px^{-1} . Therefore, we are able to classify hailstones down into the
small up to a minimum size of 3–6 mm bin size, which is a significant improvement compared to the minimum size of 220 in
Soderholm et al. (2020). The drone-based hail survey in this study mm from Soderholm et al. (2020). Here, the survey was
performed on a soccer field with a visually homogeneous background, and an excellent drainage of water. A main difference
to the approach of Soderholm et al. (2020) is the technical setup to estimate the size of the identified hailstones. Instead of
115 using an additional computer-vision-based method, we here use only use the data from the deep-learning algorithm to
directly estimate the hail sizes and shapes. In addition, we present an approach to address the major problem of the drone-based
method, which is the melting of hailstones on the ground before the aerial images are captured. The idea to tackle this drawback
is to introduce several identical, consecutive drone flight missions above the same area to capture the shrinking hailstone sizes
and derive the rate of melting. This will allow, to a certain stage, the melting rate is estimated by capturing the shrinking of
120 the hailstones from images of successive drone flights. This allows to approximate the expected largest hail sizes dating back
to at the start of the hail fall, if the exact times of the storm passage and images are known.

In Sect. 2 the end-to-end chain methodology is presented, starting from with the data collection procedure, the equipment
used a description of the equipment and details about the image data acquisition, followed by the post-processing and the
automated task of hail object, the hail detection with deep-learning algorithms and the final retrieval of the hail size distribution.
125 The results and performed investigations resulting hail size distributions, performance of the model and melting rate estimation
are described in Sect. 3. Further discussions to set bring the findings in a broader context are presented in Sect. 4. Conclusions,
ideas and suggestions for future analyses are given in Sect. 5.

2 Data and methods

Here we first go into the challenging part of the hail image data collection process (Sect. 2.1) and then provide an overview of the technical devices (drone, camera system and aerial mapping strategy) used (Sect. 2.2). An introduction to the In this study we use a deep-learning (Convolutional Neural Network) based method (Detectron2 framework, Wu et al. (2019)) method to automatically detect hail objects in the processed image data record is presented in Sect. 2.3. The hail detection and size estimation approach is evaluated based on a validation and a individual hailstones in aerial images of hail. A subset of the images was annotated by a human expert and served as a training, validation and test data set. Hereby we follow Furthermore, the test data set was annotated by two additional independent experts to objectively estimate the performance of the model. The method follows the *HailPixel* procedure described in Soderholm et al. (2020) with some slight adaption that are mentioned briefly below. The *HailPixel* technique that applies a two-stage approach, combining machine learning for finding the center hail pixel and consisting of a machine learning technique to identify the center pixel of each hailstone in the image and a computer vision (CV) for an exact hail edge detection on the image lightness in the HSL (Hue, Saturation, Lightness) color space approach to detect the edges of the individual hailstones based on pixel lightness values. During a preliminary test phase in our study, the two-stage approach from Soderholm et al. (2020) was compared to a one-stage method using solely a deep-learning instance segmentation model based on Mask R-CNN. It was found, that the to detect individual hailstones and estimate their sizes. The size estimation based on our the one-stage method led to yielded better results for this specific hail case than our data compared to the two-stage approach.

In particular for small hailstones, the pixel lightness values were much lower. Here we therefore focus on the one-stage approach.

2.1 Data collection and the experience from chasing hailstorms

A major challenge of drone based drone based hail photogrammetry is the collection of data. Therefore we here briefly describe our strategy to prepare the data collection process. Hail producing thunderstorms are highly localized phenomena and falling hail melt melts quickly on the surface due to high (summer) air and soil temperature and sometimes strong rainfall following directly after the hail. Thus, to eneounter intercept a thunderstorm, the drone operators need to be on site before the arrival of the storm. Therefore, the availability of good suitable nowcasting products and experienced interpretation are highly important. Aside from the meteorological challenges, the practical difficulties are even more pronounced. To obtain best possible quality of aerial images, we focused on places where we were confident to encounter fresh cut meadows. Public soccer fields turned out to be most promising target locations, which can be easily identified in interactive maps while being on the road, e.g. on <https://map.geo.admin.ch/> (SwissGeoportal, 2023). In addition, major parts of the hail prone areas were scouted in advance to determine potential locations to intersect a specific storm cell and familiarize with the local traffic routes.

For the preparation of the data collection process, different numerical weather prediction outputs have been consulted. We aimed at situations where the NWP models showed supercell favoring conditions, i.e. high moisture content, favorable wind shear conditions, degree of instability (CAPE) and the potential for triggering by meteorological forcing or by the terrain (s. for

~~instance?~~ for details about storm dynamics and the prediction of convective storms). During days with ~~such favoring conditions~~ conditions favorable for supercells, the drone operators were on standby in central Switzerland already in the morning hours to be ready to head towards potential regions of thunderstorm occurrence. ~~Another valuable source~~ A valuable source to identify such conditions and regions are the forecasts by ESTOFEX (European Storm Forecast Experiment, Groenemeijer et al. (2007)).

165 Our experience has shown, that at least a level 2 on the ESTOFEX internal scale needs to be issued to have a realistic chance to ~~interfere~~ intercept a hail producing cell. In general, the forecasts and evaluation of the synoptic situation across Europe provided on their website are highly valuable for the preparation process and determining, whether meteorological conditions are favorable on the next day.

On the day of an event, different nowcasting and observational products were used. Most importantly, the operational radar

170 images produced by MeteoSwiss served as a baseline to identify storms and nowcast the upcoming minutes to hours. ~~Hereby,~~ The 3-dimensional reflectivity information is crucial to not only identify the cell itself but to further estimate the strength and exact location of a potential hail core. Within the operational radar products, POH and MESHS was used. Our experience has shown that for promising results, POH needs to be 100 % and MESHS should reach stable values above 220 mm. Furthermore, satellite images and lightning information, e.g. lightning jumps (Schultz et al., 2009; Chronis et al., 2015; Nisi et al., 2020),

175 help to focus on intensifying regions within the developing storm cells. Finally, real-time hail reports from the public can give a hint about the size of the hail that can be expected and to fine tune the final decisions for a ~~successful hail core punch~~ suitable location.

Following this strategy and using the tools mentioned, two drone-based hail photogrammetry surveys could be performed during five event days in 2021. In this study, we present an analysis of the data collected on ~~the 2021-06-20~~ 20 June 2021

180 to demonstrate the methodology. The data from the second available event ~~can not~~ cannot be taken into account because of low quality of the data. In particular, both, the light conditions and the background (longer grass on the soccer field) were not optimal and thus the data can unfortunately not be used for an in depth ~~analyses~~.

~~We further want to mention as a disclaimer that for a successful hail core punch it is crucial to react fast on the basis of the instantaneous knowledge of the meteorological situation, but at the same time quick decisions can lead to a miss of the hail core. Therefore hail chasers should be resilient, have lot of patience and enthusiasm to catch the perfect storm and keep in mind that storm chasing involves potential severe risks, including injury from large hail and extreme winds. In addition, traffic conditions can be dangerous due to heavy precipitation and strong winds. Safety should be the priority during storm chasing experiments. Preparation of potential shelter spaces and escape routes is recommended in case of worst-case scenarios~~ analysis.

185

2.2 Drone operation and image processing

190 The aerial hail photogrammetry missions were performed with a DJI Matrice 300 RTK drone equipped with a Zenmuse P1 camera system, that has a full-frame sensor (45 megapixel) stabilized by a 3-axis gimbal and a focal length of 35 mm. The synchronization of the camera, the flight controller, the RTK (Real Time Kinematic) GPS module, and ~~gimbal takes place at the microsecond level and~~ the gimbal is done on a temporal resolution of microseconds and thus ensures a high accuracy of the image data.

195 ~~Studies such as Guidi et al. (2020) or Fawcett et al. (2019) showed that a frontal and side image overlap between~~ In a first
step, the individual images captured by the drone have to be combined into an orthomosaic. An orthomosaic is defined as
a composite of multiple aerial (airborne or space-borne) photos that are previously processed to remove inherent distortions
caused by the geometrical properties of the lenses (airborne photos) and the earth's curvature (space borne satellite images).
Thus, the processed individual pictures and the resulting composed orthomosaic is distortion free and exhibits a true scale that
200 allows to estimate the size of the objects within the photo. To generate an orthomosaic an image overlap between 70 % and 80 %
is within an optimal range to produce an orthomosaic. An orthomosaic is a photogrammetrically orthorectified image product
that has been mosaicked from an image collection, correcting for geometric distortion and color matching the image data to
create a seamless mosaic data set. The large overlap and the image redundancy usually allows for an efficient elimination of
erroneous matches, which in turn improves the reliability of the 3-dimensional point cloud (3D model based on collections of
205 individual points plotted in 3D space). For our performed flight missions is required (Guidi et al., 2020; Fawcett et al., 2019).
Here we use an image overlap of 70 % for both sides (frontal and sideways) ~~was applied.~~

The ~~automated flight with the DJI Matrice 300RTK drone was planned from~~ flight pattern was programmed using the DJI
Pilot 2 application ~~as~~. We defined a lawnmower (boustrophedonic) flight path without cross-hatch. ~~Due to restrictions of the~~
~~DJI control software, the minimal possible flight altitude was~~ with a flight altitude of 12 m above ground. ~~As demonstrated~~
210 ~~by Soderholm et al. (2020) or Bemis et al. (2014), a slow horizontal flight speed reduces the motion blur. A (minimal possible~~
altitude) and a flight speed of 1 m s^{-1} ~~was programmed to keep~~. A low horizontal flight speed is necessary to reduce the mo-
tion blur (Bemis et al., 2014; Soderholm et al., 2020), which is within one image pixel. ~~The image processing to produce a~~
~~high resolution georeferenced orthorectified image (hereafter called simply orthophoto) from the survey area was done with~~
in our case and leads in general to small overestimations ($< 1.5 \text{ mm}$) of the hail dimensions. The orthomosaic (or orthophoto)
215 is generated using the open source software OpenDroneMap (ODM, OpenDroneMap (2020)). ~~It is able to turn simple~~ This
software can convert 2-dimensional images into: classified point clouds, 3-dimensional textured models, georeferenced or-
thorectified imagery or georeferenced digital elevation models. ODM makes use of OpenSfM (mapillary, 2020), which is a
structure from motion (SfM) library written in Python on top of OpenCV (Bradski, 2000). The library ~~serves as a processing~~
~~pipeline for reconstructing camera poses~~ can be used to reconstruct camera positions and 3-dimensional scenes ~~from multiple~~
220 images based on multiple images (mapillary, 2023). Here we make use of ~~some~~ the basic modules for SfM: Feature detection,
feature matching, minimal solvers.

The orthophoto construction can ~~be broken down~~ can be divided into the following main steps:

- Identification of matching points between the images.
- Reconstruction of the camera perspective and the position of each image for quality check and subsequent computation
225 of the 3-dimensional coordinates of the matching points.
- Derivation of a DEM (digital elevation model) by using a reduced point cloud in 3-dimensional space.

- Construction of the orthophoto ~~of the survey area~~ by applying the DEM to ~~spatially project every image pixel~~ the spatial projection of each image point.

The first flight ~~mission after the passage of the hail core of the supercell started~~ started at 14:37:28 (UTC), which is about 230 9.5 min after the start of the hail fall. Within 3:51 min a total of 116 images were taken ~~at a constant altitude of 12 above ground level~~. Each image has a resolution of 8192×5460 pixels ~~and was captured at~~. The camera has a fixed focal length of 35 mm focal length with a manual set and for this mission we selected an exposure time of 1/1000 s, an aperture of $f/5.6$ and a light sensitivity value of ISO-25600 ~~for the applied gain by the camera sensor~~. The resulting GSD of 1.5 mm px^{-1} ~~is good enough to visually detect hailstones~~ > 5 allows to detect hailstones down to the 3 – 6 mm and thus also the smallest size classification of hail (?) bin.

The quality report A standard output of the ODM ~~processing of the 116 survey images revealed the reconstruction of software is a quality report~~. The report gives a total of 14.916.215 reconstructed dense points and a mean GPS error of 0.34 m. The ~~total hail area coverage of the orthophoto within the soccer field as presented in orthophoto covers an area of 750 m² (see Fig. 5(a) is 750~~. ~~By inspecting the computed digital terrain model of the area, a maximal change in elevation~~) that shows an elevation change of 0.5 m is found. ~~For an independent verification of the GSD,~~ Multiple reference objects (~~s-see~~ Fig. 5(b)) ~~were~~ placed on the soccer field ~~before the drone image capturing started~~. Those are used for an independent verification of the GSD. These reference objects were laminated printouts of geometric shapes in black and white, e.g. circles ~~of diameter with a diameter of 10 mm and squares with side lengths of 75 mm~~. ~~Cross checking of the 10 white circles yielded a diameter between~~ The white circles consists of 6 and to 7 pixels within the orthophoto, equivalent to ~~the metric range a diameter of 9–10.5 mm~~. Due to a 245 slight overexposure in combination with the motion blur, the black circles on white background appeared much smaller ~~than the white ones on the black background~~.

2.3 Object detection and size estimation

Object detection is a ~~technology related to computer vision and image processing that tries to detect instances of semantic objects of a certain class~~ computational method to automatically identify and locate different objects or semantic classes (e.g. 250 ~~cats, dogs, cars, buildings, etc.) in digital images and videos~~. Generally, the methods for object detection fall into either neural network-based or non-neural network-based approaches. ~~A good overview about trees, bicycles, faces) within an image or a video~~. A comprehensive overview of the techniques and developments in object detection over the last two decades ~~is shown in the road map of milestones in object detection by Fig. 2 can be found~~ in Zou et al. (2019). In recent years, many of the latest available neural network detection engines (e.g. AlexNet, VGG, GoogleNet, ResNet, DenseNet) have been applied to 255 object detection. For example, the Mask R-CNN (He et al., 2020), as one of the state-of-the-art models for instance object segmentation ~~tasks, uses the ResNet(He et al., 2016) detection engine~~. ~~This residual learning framework was,~~ uses a Residual Neural Network (ResNet) detection engine described in He et al. (2016) and is designed to simplify the training of substantially deep neural networks.

We used the deep-learning toolbox Detectron2 from Wu et al. (2019) as a starting point to train a model for visual hail recog-
260 nition. Its flexible design makes it easy allows to switch between different tasks such as object detection, instance segmentation
or panoptic segmentation. It has provides built-in support for popular data sets like the MS COCO (Microsoft Common Objects
in Context) described in Lin et al. (2014) and many backbone combinations of contains features from Faster/Mask R-CNN:
ResNet (Residual Neural Network) in combination with FPN (Feature Pyramid Network), C4 (FPN), Convolution 4 (C4)
as single scale feature map, or dilated convolution. Further a dilated convolution technique. Furthermore, Detectron2 provides
265 ready-to-use baselines with pre-trained model weights. One Here we use one set of those pre-trained model weights on the
MS COCO data set is used to train a new model on a custom designed hail class. It should be mentioned, that the training on
one class always requires at least a second class, namely for hail detection only. Thus, we only have two classes, namely hail
and the image background. Ideally for the model to be as general as possible in the detection of hail, it would be necessary to
train against various background types. Obviously, with only one captured hail event trained on a certain background (e.g. The
270 model is trained using data from a single event with grass in the background (soccer field). In order to generalise the model
and apply it to additional data with different backgrounds (less homogeneous grass field, crop fields, concrete surface), the
model should be retrained with additional data. However, not all backgrounds are suitable, e.g. on a concrete surface (a public
parking) the model performance will change (likely decrease) on a different background. hail would melt much faster due to
high solar irradiation that is likely prior to thunderstorms.

275 2.3.1 Image data preparation

~~The ODM software allows to directly export the originally produced GeoTIFF format of the orthophoto into an uncompressed
PNG (Portable Network Graphics) image format. For further processing only the PNG version of the orthophoto has been used.
The large file of width~~

2.3.1 Image data preparation

280 The orthophoto exhibits a resolution of 24500 px and height by 22000 px has a storage size resulting in a total of 5.39×10^8
pixels and a disk space of about 2 GB and a total number of 5.39×10^8 pixels. The ODM software provides different output
formats for the orthophoto. Here we use a PNG (Portable Network Graphics) format for the subsequent analysis. As shown
in Fig. 5(a) the orthophoto does not cover the full rectangular area in the image, thus the area that will be analyzed by the
object detection algorithm consists only of approximate entire image size, reducing the total analyzed image pixels to about
285 5×10^8 px. Given Thus, given the GSD of 1.5 mm px^{-1} , the area size reaches entire image covers an area of 750.4 m^2 .

The high demand of original orthophoto is divided into smaller image tiles to save computational resources during the
training of the Mask R-CNN makes it unavoidable to work with smaller image tile files. Several tests have shown that an
image tile model. A reasonable compromise is a size of 500×500 px is a reasonable compromise. Therefore the orthophoto
was divided into 2156 PNG image tiles. Later, a random selection of those image tiles was applied to assign tile images to
290 train (150 images), validate (33 images) and test (33 images) the model (s. Fig. 5(e)). The idea behind is to for each tile. We
use 10 % of all available image randomly selected tiles as reference data . This yields a total of (216 images and those were

again tiles). This reference data is further divided into 70 % for training and the remaining bulk equally split into (150 tiles) and 15 % each for the validation (33 tiles) and test data. These three data sets of images are further processed with (33 tiles) respectively. These data sets are visually analyzed by an expert A, and all hailstones are annotated using the Computer Vision and Annotation Tool (CVAT, Sekachev et al. (2020)) to manually annotate all clearly visible hailstones and to export the final annotation data set. CVAT supports multiple annotation formats, including the COCO format that is a good choice for the Detectron2 framework. The resulting annotation files are JSON (JavaScript Object Notation) based and store information about each image tile. This includes the path, width, height, annotation identifiers of the hailstones and the polygon coordinates defining their binary instance segmentation masks. Overall a total of 937 hailstone annotations are contained in the training, the training data set contains 937, the validation data 249 and the test data set, 249 in the validation set and 215 in the test set. In these annotation data sets all hailstones were visually identified by a human expert A and the identified hailstones were used as annotations during the training and validation of the neural network. To account for differences in the visually determined annotations, two more human experts (B and C) annotated the test data set consisting of 33 tile images. Thus independently, the test data set is created by three independent experts annotated by the experts B and C are used as a independent data source to assess the model prediction performance.

2.3.2 Hail detection and size estimation - training, validation and testing

The main concept behind deep-learning models is to split the reference data set into a training, a validation and not used during the training and validation process nor affects the hyper-parameter adjustments and can be used as a good benchmark against the CNN results a test data set. The training data set is used to estimate the model parameters. Within the training procedure, a validation data set is used to prevent over fitting and to assess the evolution of performance indicators during the entire training run in steps of 100 iterations. Furthermore, an independent test data set is necessary that serves as a truth against which the model results (applied to data not contained in the reference data set) and thus the model performance can be assessed. As mentioned before, we use independent test data sets where hail is visually detected by three experts (see Fig. 9).

2.3.3 Hail detection and size estimation - training, validation and testing

A NVIDIA GeForce RTXTM 3060 Ti was used to efficiently train the Mask R-CNN model on the custom hail training data set. This GPU model has 4864 CUDA (Compute Unified Device Architecture (CUDA)) cores and in total 8 GB GDDR6 RAM available. A default configuration of Detectron2 is used for a first estimate of to estimate a first set for the hyper-parameter tuning. For the hail detection training the default backbone network (ResNet) was applied and the pre-trained model on We started with a base model that is pre-trained using the MS COCO data set used a Resnet and FPN combination. The large based on ResNet and FPN. The MS COCO data set consists of about 2×10^5 annotated images with a total of 80 different object classes and it is thus an ideal starting point to train deep-learning models to recognize, label, and describe objects.

A set of 16 training model runs («run-0» to «run-15») going through several standard different training runs (run-0 to run-15) were performed to assess various hyper-parameter combinations (s. see Table 1) were conducted on the GPU device to find the most suitable trained model. Each run consisted of 3000 training iterations. With the use of 1 GPU loaded with

Table 1. Overview of the performed variations of Range tested for the 3 hyper-parameters: Learning rate (LR, 1row), γ value (2row γ) and batch size (BS) per image(3row). The hyper-parameter combination of the model with the lowest validation loss after 3000 training-iterations are highlighted in redbold font.

LR	0.0001	0.00025	0.0005	0.001
γ	0.1	0.5		
BS	128	256		

325 . Here we only vary the three hyper parameters learning rate, the gamma value and the batch size to show a concept of
proof for automatic hail detection. For detailed information about the concept and additional available parameters, we refer to
(Schmidhuber, 2015; Wu et al., 2023). These training runs were performed for each of the 150 image tiles in the training data
set. Using two images per batch and 150 training images in total, on 1 GPU, a total of 75 training iterations are needed for
batches are needed which represents one epoch time. Thus 3000 iterations translate into, i.e. to iterate through all available
330 image tiles. We then performed 40 epoch times for each of our performed runs. The number of epochs needed highly depends
on the diversity of the data, and as ours consists only of one object class, the chosen 40 epochs are enough resulting in a total
of 3000 iterations.

The internal model evaluation period was set to During an individual training run, the validation is done every 100 iterations.
This means, that there are Thus, for one training run with a total of 3000 iterations we obtain a temporal evolution of the
335 scores along 30 available points along the iterations where the performance of the model is automatically back-tested against
the validation data setpoints. Figure 6 compares shows the progress of total and loss and the validation loss for the all 16
performed training runs. The thick bold lines show the run which had training runs performed. The bold lines depict the
run exhibiting the lowest validation loss after 40 training epochepoch times. To chose the best model, we performed a more
detailed evaluation of the model runs by means of commonly used metrics in object detection. The accuracy of an object
340 recognition model depends on the quality and number of training regions, the input image data, the modelparameters, and the
accuracy requirement threshold. Usually, the IoU (Intersection over Union) ratio is used as a threshold to determine whether a
predicted result is a true positive (TP) or a false positive (FP)

To assess the performance of a model, diverse metrics are available. A single score (i.e. performance metric) does provide
the model performance from a certain perspective and thus different scores should be taken into account. A score compares
345 the predicted result with the truth based on a confusion matrix (Wilks, 2011). In image classification the predicted results of
an individual feature (i.e. hailstone in our case) usually does not exactly match with the truth (the same hailstone in the test
data set) but the area of overlap can vary. We therefore use the Intersection over Union (IoU) ratio. The IoU ratio is usually
the overlap between the surrounding rectangle around a predicted object and the surrounding rectangle around the same object
in the reference annotation data set. In this study, defined as the ratio between the overlap and the union of the bounding box
350 around the features in the predicted result and the truth. In our case we use the IoU retrieved from the binary mask areas and
not from the surrounding rectangles. Following the standard COCO evaluation procedure, the instance segmentation mask (i.e.

the one segmentation mask for each individual feature) instead of the bounding box to compute the IoU ratio. The IoU ranges from 0 to 1 and a ratio of 0.5 is used to define a correct prediction and thus interpreted as a true positive (TP) result. Predicted results with a IoU less than 0.5 are thus false positive (FP) and if no results is predicted for an existing feature in the truth, it is depicted as false negative (FN). Following the standard COCO evaluation procedure, the set of IoU ratios ranges from 0.5 to 0.95 in steps of 0.05. The minimum IoU value for a matching detection (IoU ratios for a TP result) is 0.5.

The normal procedure when training a deep learning model is to split the reference annotation data into a train and a test set. Because we want the test data set to be locked down until we are confident enough about our trained model, we do another division and split a validation set out of the train set. In this scenario we end up with three data sets. Usually we want to compare how well the model is performing on the validation set during the training, in order to know when are we at risk of over-fitting the model to the training data. In the end, the final evaluation of the model performance should be computed on the test data set, as the model training was totally independent from it. Further we used the test set to investigate the discrepancies between three professional experts, who annotated the hailstones in those images (s. Fig. 9).

The model «run-3» was selected for the final hail detection and size estimation. Every single tile image was pushed through this Mask R-CNN model version («run-3») and the binary masks of all found hail objects were saved in separate Python structures linked to the individual images. Regarding the full orthophoto area (Fig. 5(a)), split into the 2156 tile images, the Mask R-CNN model classified 18209 objects as hailstones. A few large objects (e.g. leaves) were wrongly classified as hail and manually removed to guarantee a correct representation of the largest hail size bins in the distribution ranges from 0.5 to 0.95 in steps of 0.05.

In pattern recognition, information retrieval, object detection and classification (machine learning) machine learning, precision and recall (Eq. (1) and Eq. (2)) are standard performance metrics (Powers, 2020) that apply to data retrieved from a collection or sample space. Precision $[0, 1]$ is a measure of result relevancy, while recall $[0, 1]$ is a measure of how many truly relevant results are returned. A model system with high recall but low precision returns many identified objects, but most of these objects are incorrectly labeled (False positive) when compared to the validation labels. On the other hand, high precision but low recall is just the opposite, where only few objects are identified and most them are labeled correct, when compared to the validation labels. An ideal system with high precision and high recall will return a realistic amount of positive results. The commonly used (Powers, 2020). Precision depicts the number of true positive results divided by the total number of positive results. Recall refers to all true positive results divided by the number of all samples that should have been classified (i.e. as visually identified by the experts in the test data set in our case). Precision and recall can be combined in the $F1$ score in Eq. (3) combines precision and recall metrics into one unified measure and is designed to handle imbalanced data effectively (Van Rijsbergen, 1979; Goutte and Gaussier, 2005). The $F1$ score results in values from 0 to 1 where 0 indicates extremely poor performance and 1 refers to a perfect performance of the model.

$$Precision = \frac{TP}{TP + FP} \quad (1)$$

$$Recall = \frac{TP}{TP + FN} \quad (2)$$

$$F1 = 2 \cdot \frac{Precision \cdot Recall}{Precision + Recall} \quad (3)$$

385 With regard to Fig. 7, a reasonable compromise between high precision and high recall values for «run-3» was found at a confidence threshold of around 0.9. At higher threshold values the gradient of the recall decrease starts to increase. The maximum of the $F1$ score is not reached there but is reasonably close and some compromise has to be taken. The curve signatures are found to be similar for the validation and Here we prioritize the precision and aim at a large portion of correct
 390 detection (TP) of hailstones and low false positive results (i.e. hail detected by the model but not present in the test data set results, however the latter are slightly lower either by chance or the fact that the test data set was not used to find the optimal MASK-RCNN model run. At the model confidence level). Thus, as a trade-off some hailstones are missed (FN) and the selected threshold does not exactly correspond to the optimal $F1$ score. A reasonable compromise between precision and recall is found at a hail confidence threshold of 0.9 for *run-3* (see Fig. 7) where $F1$ is close to 0.8 (0.85) when evaluating
 395 against the test (validation) data set. The appearance of 4 four groups in the two plots of Fig. 7 is due to the quadruple variation of the learning rate four different learning rate values tested (Table 1).

Looking deeper into From the 16 different training runs, *run-3* is chosen as the model to apply to the orthophoto for automatic hail detection. Thus, (*run-3*) was applied to all available image tiles (2156) and the instance segmentation masks of each detected hail object was saved in separate Python structures linked to the individual images. In total, 18209 objects were
 400 classified as hail. A visual evaluation of the largest objects revealed some leaves that were incorrectly classified as hail and therefore manually removed to guarantee a correct representation of the largest hail size bins in the distribution.

In the validation data set consisting of with 249 annotated hailstones, we find a TP number of 237 and a FN number of are
 TP and 12 which gives a miss rate or are FN resulting in a false negative rate ($FNR = FN / (FN + TP)$) of 4.8 %. For the test data set (with 215 hailstones), 198 are TP reaches 198, FN count and 17 which yields to $FNR = 7.9 FN$ which yields a
 405 FNR of 7.9 %. The An additional performance metric used to describe the accuracy of a model is the mean average precision, that is calculated over the whole IoU range, for the (mAP). In short, mAP depicts the average relationship between precision and recall over all IoU classes (from 0.5 to 0.95). The mAP for the validation (test) data set results in 0.53 (0.50) for the 90 % hail confidence threshold reaches 0.53 (validation data set), respectively 0.50 (test data set). Figure 8 gives an advanced view on hail confidence threshold. In addition, Figure 8 shows the number distribution of the IoU of the for all true positive matches
 410 (hail confidence level $C_i \geq 0.9$), again for both within the validation (blue bars) and the test (green bars) data sets. A large set. The majority of the hail-IoUs lie above 0.7, indicating a good match between the predicted hailstones and the truth. For the test data set a bi-modal distribution shape is found with peaks around 0.76 and 0.86.

As mentioned earlier, a pre-evaluation of the performance of the model capability to produce a reliable HSD has been done by generating two more reference data sets from the 33 test tile images. This also gives the opportunity for a certain evaluation

415 of the references themselves by analyzing the differences between the independent hail annotations. From in the beginning, the
test data set is visually classified by three independent human experts. This allows assessing the uncertainty of the test data set
resulting from the visual detection of the hailstones. The hail size (in terms of major axis length) is derived from the annotated
polygons in the test data set and the sizes are derived and together with the model results the comparison between four hail
size distributions is shown in Fig. 9. For all shown hail size distributions later, model output. The resulting HSD with a bin size
420 of 3 mm is taken. The distributions from the model, are presented in Fig. 9. It shows that expert B and expert C peak in have a
peak number of hailstones within the 6–9 mm major axis hail size bin, where also the median (9) is found. Against this, the
peak bins. The median value of these experts assessments is 10.5. In comparison, the highest number of hailstones and the
median (10.5) slip one bin to the right in case of the distribution based on expert A annotations value of expert A are found in
the next higher bin class. Overall the discrepancies are largest for the smallest hail major axis size bin (3–6 mm). This probably
425 indicates that the orthophoto resolution limits the is a limiting factor for reliable identification of those such small hailstones by
human vision. The clear visibility of many small hailstones suffers from a reduced lightness due to clearer ice and a translucent
background. In the main results visual classification as this size class suffers from low brightness and translucent background
(see also Sect. 3 and discussions (Sect. 4) we will elaborate on the lightness issue.

3 Results

430 In this section the most important results are presented by means of the complete time-integrated we first present the resulting
hail size distribution from the 750 orthophoto area of the first of five drone-based hail survey flights after the passage of the
supercell on June first flight performed on 20 , 2021. The derived distribution is very smooth and provides, for this specific
case, a more comprehensive picture of the HSD than with smaller devices, especially of its right tail (largest hailstones). June
2021. We compare the HSD retrieved from the photogrammetric approach presented above to the HSD retrieved by four close
435 by hail sensors (Sect. 3.1). Subsequently, we assess the sampling error of hail sensors having an observational area of 0.2 m²
with a sub-sample of data retrieved from the drone observation from an area of 600 m² (Sect. 3.2). In Sect. 3.3, we estimate the
melting rates of hail on the ground based on the evolution of the HSD from all five successive flights.

3.1 Estimation of the HSD

3.1 Estimation of the hail size distribution

440 The number distribution (logarithmic view) of the hailstone major axis lengths is shown in the histogram of Fig. HSD estimated
from the aerial photogrammetric data is shown in Fig. 10. The distribution contains a total number of 18209 hailstones, and
the size refers to the major axis determined by the machine learning algorithm. 45 hailstones are larger than 30 mm with the
largest size being 39 mm. The mode of the distribution lies in the 6–9 mm bin. Only a few hailstones are larger than 21 mm.
The closest automatic hail sensor HS2 recorded 9 hailstone impacts with a maximal diameter impacts within 3 min and a
445 maximum hail dimension of 14 mm in a time span of 3 (Fig. 4). The duration of the event at the location of the drone survey

was ~ 9.5 min. Relatively seen, much more small hailstones were measured by Estimated duration based on the neighboring hail sensors range from 3 min for HS2 (likewise for HS3 and, 13 min for HS4) then by the drone and 16 min for HS3. The up-scaled density of hailstones detected by the HS2 sensor is 45 hailstones per m^2 , compared to 24 hailstones per m^2 (average) for the orthophoto hail survey area. Possible reasons include, that drone measurements are affected by complete melting of small hailstones and the overlooking of hailstones due to too low lightness or hiding in the grass surface. The spatial variability of the hail size distribution can also have an influence, given that the samples were not taken at the exact same location. Our data illustrates the presence of quite large time span differences for the impacts on the sensors. HS3 recorded a hail duration of 52.5 (probably it was hit by another hail cell shortly after the passage of the main supercell). The hail duration at HS4 (13) was closest to the one estimated at the soccer field: ~ 9.5 .

The HSD measured by drone-based aerial photogrammetry is shown on Fig. 10. It is based on 18209 hailstones, which is substantially larger than any sample measured by the near-by automatic hail sensors (Fig. 2(d)). Thus, it provides a much more comprehensive picture of the shape and upper tail of the HSD. In the orthophoto area most hail objects (6663) were classified in on average as retrieved from the drone data. This might be related to the 6–9 bin. Within the large survey area of inherent spatial and temporal variability of hail as the automatic hail sensor is located in a distance of about 750, 45 hailstones are found to be greater than 30770 and the largest hailstone size reached 39 mm. These largest hail sizes are not captured by the hail sensors, as large hailstones are more sparsely distributed. In the subsequent Section 3.2 we try to assess the sampling error of hail sensors by showing how many random virtual placed hail sensors would capture hailstones larger than a certain threshold and also the probability for a no-hit event is investigated.

We note that the mean lightness value m downstream of the area observed by the drone. In addition, the sensor detects the hail directly during the event, whereas the drone data is collected after the hail stopped to avoid the drone being damaged. Therefore, the drone data is affected by melting processes and thus tends to underestimate the hail size and in particular the number of small hailstones. Furthermore, small hailstones might not be detected within the drone data as they might partially be obscured by the grass and by low differences in the lightness values compared to the background. Lightness values come from the HSL (Hue, Saturation and Lightness) color space and range from 0 to 255. Mean lightness values (Fig. 10, orange line) increases with increasing hail size. The lightness value is shown here as a digital value in the HSL color space. The theoretical maximum is 255 and the highest value is just below 250. For the very small hail the mean lightness shrinks for the 3–6 mm hailstones drop below 180 and thus becomes gradually which is similar to the lightness of the background. Edge detection methods based on the lightness value background. Size estimation based on edge detection methods that use lightness values alone, such as proposed in the work of Soderholm et al. (2020), will have difficulties in finding the correct hail pixel edges. Soderholm et al. (2020), can thus not be applied.

The same drone-based HSD as in Fig. 10 is shown again with as a function of the probability density in Fig 11(a). There additionally the shape is approximated by a Γ gamma probability distribution function (PDF). In general, the gamma PDF was also found to be most suited to hailstone is used to approximate the empirical HSD. The gamma PDF is most suitable to characterize the distribution of the hailstones major-axis lengths by other case studies, e.g. Ziegler et al. (1983); Fraile et al. (1992). In our case, as shown by Ziegler et al. (1983) or Fraile et al. (1992). Overall, the gamma PDF slightly underestimates the

probability density of the peak, but still a quite smooth fit is achieved. The median size was found to be closely follows the empirical distribution retrieved from the drone data with a median of 9 mm (s. and a slight underestimation of the peak (see Fig. 11(a)). The probability density of the projected hail aspect ratios shows, indicate that the majority of hailstones show have equal axis lengths (Fig. 11(b)) -and 75 % of the hailstones have projected aspect ratios higher than 0.75.

485 3.2 Assessment of sampling ~~Sampling error of within automatic hail sensors using sensor data with respect to~~ drone-based data

In the previous section, we showed that drone-based aerial photogrammetry can provide a more comprehensive picture of the tail of the HSD than hail sensors, due to its larger sampling area. We note that the HSD is considered at the scale of a single hail cell. The simulation performed in this section assumes that the full HSD is known and given by the drone-based hail data.
490 Based on this assumption, we investigate this section, we estimate the probability that a randomly placed hail sensor on the orthophoto area is not hit at all or is hit by a stone larger than a given size. To do so, we randomly placed hailstone of a certain size. 10000 virtual areas hail sensors with a size of 0.2 m^2 were distributed across an area of 600 m^2 within the orthophoto (blue circles in the orthophoto of Fig. 5(d)) of the same size as the hail sensor (0.2) on a 600 area from the orthophoto. For each virtual areasensor, the HSD was derived. The and the individual Kernel density estimates (KDE, gray lines) are plotted
495 shown in Fig. 12(a). The KDE could be was obtained from 7817 virtual sensor areas. The remaining 2183 sensors had too few impacts and the KDE could not be estimated did not have enough virtual impacts to estimate the KDE. The distribution from the whole entire 600 m^2 area is shown by the blackline in black, and the respective quantiles (Q25, Q50 and Q75) from all the virtual sensors as red lines in blue, red and green.

The data from the large random generated virtual sensor samples reveals that Within all virtual hail sensors only 45 hailstones
500 with a size larger than 30 mm are observed and thus only 0.3 % (34 out of 10000 virtual sensors) record hits larger than 30 mm,) of the virtual sensors exhibit an impact of such large hail. 9.9 % (988 sensors) record hits) of the virtual sensors observe impacts from hail with a size larger than 20 mm and 65.8 % (6576 sensors) record hits) from hail with a size larger than 10 mm. Moreover, the probability of a no-hit for an individual sensor was found to be about that a sensor records no impact at all is 4.7 %. While we found 45 hailstones > 30 , the probability for a sensor to record such a large hailstone is only 0.3.

505 In Fig. Figure 12(b) a distribution calculated from the largest hits on shows the distribution of the largest hailstone observed by each virtual sensor is shown with markers of certain percentiles. The median value reaches 12 mm and the 95th percentile is at a major axis length of (Q95) corresponds to 24 mm.

Figure 12(c) shows the histogram from distribution of the number of hits per virtual sensor areas hailstones observed by all virtual hail sensors and compares it with the point measurements of the 4 closest number of observed hailstones within the four
510 physical hail sensors. The locations of those sensors in context with the drone observations on the soccer field is shown on the map in Fig. 2. All those sensors were crossed by the 3. All physical hail sensors were within the hail path (100 % POH region (at $1 \times 1 \text{ km}$ resolution) of the hailstorm. Regarding the 600,

The highest probability (22 area the probability for 3 hail impacts on a small sensor area was highest (e.%, see peak of histogram in Fig. peak of the histogram). Zero hits 12(c) is given by 3 impacts on a virtual sensor. The probability for zero

515 ~~impacts (e.g. HS1 sensor, cyan line) were more likely than is 4.7% and the probability for 9 or 10 as recorded by the impacts~~
~~(HS2 sensor (blue line) and HS4 sensor (red line). The HS3 sensor towards the SSW with 33 impacts seems to be an outlier~~
~~here. Very likely, the HS3 sensor was hit by a second hail cell later, because the time interval between the first and the last~~
~~impact was 52.5, compared to 3 at HS2 and 13, blue and red line, respectively) is less than 2 at HS4. The % 32 impacts~~
520 ~~placements is impacts (12. But one must be aware that an unknown number of small hailstones were already completely melted~~
~~and not available in the data set for this investigation with the consequence of a biased histogram towards fewer hail impact~~
~~numbers) within all virtual sensors. This indicates that the spatial variability might play an important role and/or the limitation~~
~~of the drone data regarding the melting process prior to the flight might affect the estimation.~~

3.3 Melting on the ground and ~~the impact implications on the estimation of the HSD~~ hail size distribution estimations

525 ~~The use of A major limitation of the~~ drone aerial photogrammetry for measuring hailstones has a drawback – the drone cannot
~~be flown until the hailstorm has ended. This delay causes a time gap in measuring the hailstones, allowing them to melt on~~
~~the ground is its timing with respect to impact. Hail from the beginning of the event is thus already affected by melting and~~
~~decrease in size until the drone observation can take place. In this section, we try to estimate quantify the impact of melting~~
by comparing the data from five successive drone flight missions, where flights. This allows to estimate the temporal evolution
530 of the HSD could be monitored. As equally sized areas are important for this investigation, we decided to crop the area of
~~the orthophotos to the marked soccer center circle. This procedure was a compromise because a one to one assignment of all~~
~~individual hailstones between the orthophotos was not feasible in a reliable way due to small misalignments and changes in.~~
Figure 13 illustrates the shape evolution of two prominent hailstones during the melting process. Due to slight deviations in the
~~derived orthophotos and the melting process itself, the location of the the center hail pixel due to the melting and differences~~
535 ~~in the orthophotos. To illustrate this, we show the shape evolution for the five time stamps (s. Table 2) of two large, prominent~~
~~hailstones in Fig. 13. Those hailstones shrink from initially 33 to 21, respectively 25.5, during the course of 1119 changes~~
~~and leads to misalignments for an individual hailstone across the successive flights. Therefore, we only use a subset of the~~
~~orthophotos and select the area within the soccer center circle which can be unambiguously identified.~~

With a radius of 10 yards (9.15), the ~~The~~ area of the soccer center circle (263 m^2) is well defined and reaches 263 with
540 ~~a radius of 9.15. The fact that this area was covered in all 5 drone flights makes it an ideal start point to deeper investigate~~
~~the melting process. With this we are able to get a first idea how much the upper tail of the distribution degraded and thus~~
~~approximate better the ground truth of maximal hail sizes. A first observation tells us, that m. Within 18.65 minutes, the time~~
~~between the first and the last drone flight, the number of hailstones is roughly reduced decreased by 64, % in the soccer center~~
~~circle (s. (see Table 2) from the first to the fifth hail survey. The evolution of the Kernel density estimation for all five orthophoto~~
545 ~~soccer center circle cut outs is once shown with normal and logarithmic y-axis KDE retrieved from all individual drone flights~~
~~is shown in Fig. 14. From the black to the red curve we see how the peaks and tails degrade over the distinct time frames. The~~
~~peak density decreases from more than 0.038 to 0.017, while moving slightly leftward towards smaller hail size bins. Tracing~~
~~certain plateaus in the different colored distributions, A clear shift of the peak and the upper tail to smaller major axis lengths~~

Table 2. Time slots in UTC, when the aerial pictures of the soccer center circle (263 m²) were captured for the five drone mapping flights. ~~The drone image capture intervals with the camera last between 198 and 200. The time differences between the sequence of orthophotos are: 307, 273, 268 and 271. From the first to the last orthophoto 1119 s (18 min, 39 s) passed. The last column gives the number of hailstones detected within the soccer center circle for each of the five orthophotos elapsed.~~

Capture series	Start [UTC]	Stop [UTC]	Capture interval [s]	No. hail Number of hailstones
1	14:37:59	14:41:19	200	3925
2	14:43:06	14:46:25	199	3077
3	14:47:39	14:50:59	200	2511
4	14:52:07	14:55:27	200	1962
5	14:56:38	14:59:56	198	1411

550 ~~can be observed. The shift of the plateaus on the upper tail indicate melting rates in the order of magnitude of 0.5 can be deduced. This is supported by the more accurate results from an individual tracking of 48 hailstones of different initial sizes. The melting rate range, that was observed for the different hail size bins, lied in average between 0.3–0.5 mm min⁻¹. The sample size of 48 hailstones however is much too small to make assumptions on melting speed in relation to the initial hail size.~~

555 ~~By assuming a melting rate of 0.5 and a temporal delay of 9.5 (Using this melting rate estimate together with the time difference between start of hail and drone image capturing) for i.e. the largest the start of the hailstorm and the first drone flight, we infer that the initial size of the largest captured hailstone (39 mm) ,an initial size of rounded was 44 mm could be expected, which is closer to the result of MESHS (63). Most crowdsourced reports in the vicinity of the soccer field indicated sizes of a 5 from 30 coin (~3mm to 50). Golf ball sizes (~5cm) were also reported a few kilometers to the NE of the soccer field (s.mm and the MESHS estimate was 63 mm (see Fig. 2(b)). Immediate on-site measurements On site measurements by~~
 560 ~~the storm chasers during the hail event revealed maximal hail diameters between 4 and 5 maximum hail dimensions between 40 and 50 mm as well.~~

4 Discussion

565 ~~Hail forms through A major challenge for drone-based photogrammetry of hail is related to the appearance of the hail within an orthophoto. The hailstones need to show distinct differences from the background. This is not always the case as hail is formed by a combination of dry and wet growth processes, which can lead to varying densities and appearances in the ice. Dry growth results in bubbles and irregularities in the ice produces high densities of microscopic air bubbles that scatter light, while wet growth causes liquid to soak into gaps and form a clearer and higher density accretes on top of existing outer ice to form clearer ice. Hailstones can alternate between these growth grow in both regimes, leading to alternating layers of cloudy and clear ice (Allen et al., 2020; Kumjian and Lombardo, 2020; Brook et al., 2021). For the detection and size estimation of~~

570 ~~hail stones in image data, these facts are of relevance~~ Thus, for hailstones with high transparency the approach used here might ~~not work~~.

In a first step, a pure ~~First, a simple~~ computer vision approach ~~without the use of neural networks~~ (without neural networks) was tested to extract the ~~binary-segmentation~~ hail masks. The approach was based on lightness thresholds, morphological transformations and watershed algorithms (Najman and Schmitt, 1994) for image segmentation within OpenCV (Bradski, 575 2000). The success and reliability of this approach highly depended on the visual appearance of the hailstones. For larger ~~sizes~~ ~~it worked well, but with the decreasing lightness of the small hailstones~~ ~~hail exhibiting distinct lightness difference compared to the background, this approach is promising. But for small hailstones exhibiting lower lightness values~~ (Fig. 10) ~~the method produced very poor results like~~ the CV-based edge detection (~~s. see~~ Sect. 1 and 5) ~~It could be different with the appearance of hail failed. For hail events with different characteristics, e.g. with a high number of small hailstones that aggregate in~~ clusters on the ground, ~~where algorithms based on watershed~~ ~~watershed algorithms~~ could retrieve more reliable information, ~~but this needs to be tested~~.

In a second step ~~Second,~~ a deep-learning model (Mask R-CNN) was tested. ~~By now, the training of this model consisted of only~~ ~~We used~~ one single hail class ~~Performance wise, it might be worth to check if an inclusion of different~~ ~~to train the model. Additional~~ hail size classes ~~can~~ ~~might~~ improve the hail predictions and mask shapes. ~~For a simple check we propose~~ 585 ~~to simply start with two classes: small and large hail~~. The exact size threshold for separation needs to be defined, but could lie for instance at ~~In particular, a distinction between damaging and non-damaging hail with a threshold of 20 mm~~, where the potential for damage starts to rise. A thorough investigation of hundreds of ~~could be worth to test. Furthermore, additional testing of the~~ hyper-parameters ~~can lead to better results~~ ~~might increase the performance~~, but this ~~is~~ ~~was~~ out of the scope of this study. ~~If the future direction is to build a more generalized Mask R-CNN model for hail detection and size estimation, it is a~~ 590 ~~good idea to invest more into the tuning of the training and validation configuration.~~

~~Splitting~~ ~~Another technical challenge arises from splitting~~ the orthophoto into ~~many~~ smaller image tiles ~~can produce artificially cropped hailstones. To avoid this issue, which can result in truncated hailstones. This can be overcome by~~ producing overlapping tiles by the ~~maximal~~ ~~maximum~~ length of the largest observed hailstone ~~are one possibility~~, as implemented by Soderholm et al. (2020). However, ~~for sporadic large hail coverage (no clustering of many hailstones on the ground), as observed for the~~ 595 ~~2021-06-20 superecell storm, the expected corrections due to the few cropped hailstones are marginal in comparison to other errors like negative and positive false detections. Also a cropped hailstone binary mask can still lead to~~ ~~in our case large hail was sparse and, as the correct major axis length. image tiles cover large areas (500 × 500 pixels), it is safe to assume that the number of truncated hailstones is very low. Other sources of errors such as false positive detections or missed hailstones likely play a more important role.~~

600 The acquired hail images from the drone show large differences in their transparency, making it difficult to apply simpler computer vision techniques for detection and size estimation. Beside the effect of melting after hail has reached the ground that can change the color and transparency in the visible wavelength range, the microphysical growth processes in the storm determine the inner and outer structures of a hailstone. Often, analyzed hailstone slices (?) show layered patterns with alternating transparencies (clear versus cloudy ice). During dry growth, where super-cooled liquid water freezes immediately onto the

605 ~~surface of the ice particle, the probability for trapped air bubbles is high (Rasmussen and Heymsfield, 1987; ?)~~ Hailstones usually have an oblate spheroid shape with mean axis ratios close to 0.8, though they can sometimes have large protuberances (Knight, 1986) and the probability for nonspherical shapes rises with increasing maximum dimension (Shedd et al., 2021). As a consequence the hail aspect ratio decreases for larger sizes as shown in the various studied data sets (Knight, 1986; Soderholm et al., 2020; S
610 ~~Figure 6 in Shedd et al. (2021) compares their recent results on the evolution of aspect ratios with maximum hail sizes from manually measured hailstones to the results of Knight (1986). The slopes of the decreasing aspect ratios are comparable, but the absolute values tend to be lower in the hail data set of Shedd et al. (2021), reflecting possible effects by melting before the measurements were taken. Likewise with hailpads, the shape factor in the image plane can be determined with the aerial drone-based hail photogrammetry, but the estimated aspect ratios (Fig. 11(b)) may differ from in-situ measurements as published in e.g. Knight (1986); Shedd et al. (2021). The hail images show only the projected maximum and minimum axes,~~
615 ~~which may differ to the true stone axis ratios.~~

~~A few studies exist, that explore the~~ Another limitation of the drone-based photogrammetry is that melting already affects the hail before the data can be collected. The effect of melting hail in the air ~~from~~ was studied by Kumjian and Ryzhkov (2008) using polarimetric radar measurements (~~?Kumjian and Ryzhkov, 2008) or models (Fraile et al., 2003)~~ and numerical model investigations were performed by Fraile et al. (2003). Other studies by Rasmussen and Pruppacher (1982) and Rasmussen and Heymsfield
620 ~~have explored the melting of spherical ice particles falling at terminal velocity. They found that the melting rate depends on the initial size of the spheres size and the surroundings, including temperature, humidity, turbulence, and how meltwater is shed. The hailstones in our case are already on the ground, so they experience different environmental conditions compared to when they are falling through the atmosphere. We have not measured these specific conditions for each hailstone, so we cannot make any conclusions about how the melting rate relates to their initial size.~~

625 To our knowledge there are no studies ~~that~~ analyze the melting of a large sample size of ~~real~~ hail on the ground ~~after the passage of a hailstorm. Here we provided a potential method to cover this gap and potentially allow to retrieve the original HSD. However,~~ We here provide a first estimate about the melting process of hail on the ground. More in-depth investigations would be needed to retrieve more accurate results, maybe also in relation to initial hail sizes and environmental conditions like ground temperature and occurrence of rain before, during and after the hail event ~~can strongly impact the melting rate and~~
630 ~~therefore would pose some uncertainty to a reconstructed initial HSD.~~

~~Because the melting rate will be dependent on~~ In Table 3 temperature and relative humidity ~~, some measurements of those parameters in the relevant time period are shown in Table 3 for two SMN (SwissMetNet for two SwissMetNet (SMN) weather stations (Schüpfheim and Langnau i.E.) . Although the distances to the soccer field are are shown. The stations are located in a distance of~~ 5.7 km (Schüpfheim) and 20 km (Langnau i.E.) ~~the geographic locations in the same valley are somewhat comparable. In particular, Langnau i.E. is included here because it is the closest station with measurements of temperature at 5 above grass and at the ground. Unfortunately no in-situ meteorological measurements at the hail survey area of the 2021-6-20 event are present. Precipitation measurements to the soccer field. Unfortunately, no in-situ measurements are available for this event. Closest precipitation measurements from an automatic rain gauge (Station: Entlebuch) are available at a distance of 670 m to the east. There, an automatic rain gauge (Station: Entlebuch) recorded~~ 9.1 mm ~~were recorded~~ between 14:30 and

Table 3. Measurements of temperature at 2 m (T_{2m}), 5 cm (T_{5cm}), ground-level (T_{0cm}) and relative humidity at 2 m (RH_{2m}) from the SwissMetNet (SMN) weather station in Langnau i.E. (744 m a.s.l.) and measurements T_{2m} and RH_{2m} from the SMN weather station in Schüpfheim (744 m a.s.l.). ~~The temporal period is between 14:00 and 15:30 on 2021-06-20 with a resolution of 10-20 June 2021.~~

Time	14:00	14:10	14:20	14:30	14:40	14:50	15:00	15:10	15:20	15:30
T_{2m} (Schüpfheim)	23.5	23.4	23.1	21.0	19.3	20.3	19.4	18.4	18.4	18.6
RH_{2m} (Schüpfheim)	66.9	67.5	69.2	77.9	86.0	82.1	87.7	89.2	90.4	90.5
T_{2m} (Langnau i.E.)	23.4	22.9	18.9	18.4	18.1	18.4	18.4	18.4	18.7	19.1
T_{5cm} (Langnau i.E.)	22.0	21.5	17.9	17.4	17.4	17.2	16.9	18.0	19.8	21.6
T_{0cm} (Langnau i.E.)	21.8	21.3	18.1	17.4	17.5	17.3	17.1	18.1	20.2	21.9
RH_{2m} (Langnau i.E.)	71.1	75.7	93.9	96.5	99.2	93.7	90.8	94.9	96.9	92.7

640 14:40 UTC and 0.2 mm in the subsequent 10 minutes. ~~The very light precipitation continues also in the still relevant 10 minutes time slot from 14:50 until 15:00 (compare times in Table 2) with an accumulation of 0.3.~~ Thus, the ~~time-integrated HSD from the first hail survey mission with the drone was most exposed to rain. Temperatures close the ground have fallen~~ hail on the ground was exposed to strong rain, what might effect the melting rate. At the same time temperatures close to the ground decreased by about 4.5 °C between 14:00 UTC and 14:30 UTC, after the supercell passed the SMN station Langnau i.E. ~~SMN weather station. For which is assumed to be in a similar range for the soccer field. To better assess the melting process,~~ future drone-based hail surveys ~~that try to retrieve information about melting, it could be a good idea to place~~ should include a mobile weather station or some ground temperature sensors at the ~~hail measurement location to record more accurate data~~ observation site.

5 Conclusions and outlook

650 Reliable ground truth data from hail observations are rare and of high value to the hail research community. This paper ~~describes the assesses an~~ application of aerial drone-based photogrammetry combined with a state-of-the-art deep-learning object detection model to retrieve the ~~time-integrated~~ hail size distribution over a large ~~survey~~ area. The ~~ability to analyze~~ HSD retrieved from a large survey area allows to capture a ~~much more representative sample of the distribution than with other~~ representative distribution and can thus serve as a complementary source to existing ground-based ~~measurement techniques, especially for~~ the upper tail of the size distribution ~~observation networks such as automatic hail sensors and crowdsourced reports.~~

660 During a period in June 2021, ~~when~~ exceptionally strong convective ~~supercell storms occurred~~, a ~~successful data collection with the drone took place. On 2021-06-20 storms occurred in Switzerland. On 20 June 2021~~ drone-based photogrammetric data ~~from a sporadic large hail fall (no clustering) from of a hail event related to~~ a right-moving ~~classical supercell could be~~ supercell was collected near Entlebuch (Canton Lucerne, Switzerland). ~~Aerial drone imagery of the hail survey area (750 on~~ Five successive drone-based photogrammetry flights were performed above a soccer field ~~) could be captured in five subsequent photogrammetry flight missions~~ between 14:38 and 15:00 UTC. ~~We presented our approach to retrieve the hail size distribution~~

using a A deep-learning instance segmentation model (Mask R-CNN) under the Detectron2 framework. ~~A broader part of the paper dealt with the validation and testing of the model predictions~~ was trained to automatically retrieve the hail size distribution.

~~A short summary of the~~ The key results and conclusions ~~of the presented work is~~ are listed below:

- 665 – A robust retrieval of a HSD based on ~~a population size of 18209 hail stones~~ hailstones on an area of 750 m² from a single hail event with a duration of about 9.5 minutes ~~on 2021-06-20 was carried out~~ is presented. The median hailstone size was 9 mm and ~~hailstones with equal axis length (minor/major) dominated.~~ the majority of hailstones had projected aspect ratios close to 1.
- 670 – The largest ~~hail stone reached~~ hailstone was 39 mm and is substantially larger than ~~impacts on the closest hail sensors at distances between 300 and 1470 from the soccer field~~ estimates retrieved from close-by automatic hail sensors.
- A combination of hail data from different ~~applications~~ sources (drone, ~~sensor and crowdsourced~~) ~~that observe the same hail fall~~ automatic hail sensors and crowdsourced reports to observe hail on the ground improves the reconstruction of the complete HSD ~~of such an event and also helps to frame the individual limitations.~~ This will help to better compare the data also to ~~and allows to assess the limitations of each method. Furthermore, such ground truth data can help to~~ verify and further develop radar-based hail ~~products~~ estimations.
- 675 – ~~Investigations with virtual sensors can provide relevant statistical information for various applications, e.g. probability of miss rates and impacts of certain size on a small sensor measurement area~~ The analysis of virtual hail sensors placed in the photogrammetric data highlights the challenge to observe a representative sample of the HSD using a device with an area (0.2 m²) much smaller than a typical hail swath.
- 680 – The ~~decay~~ evolution of the HSD caused by melting could be monitored ~~during 18.5~~ for a period of 18.65 min by ~~performing additional drone photogrammetry flights. Melting rates in the range 0.3~~ analysing data from multiple drone flights. A melting rate in the order of 0.5 mm min⁻¹ ~~were~~ could be estimated.

The aerial drone footage of a larger field with hail is not an instantaneous picture of hailfall, but prone to different ages of hailstones after they fell on the ground. Although the time differences are just within minutes, the hailstones are in different melting stages and appear differently regarding their outer ice transparency. If the aim is to capture all of those different looking hailstones for the best possible estimation of the distribution, we find that Radar-based hail algorithms estimating the size of hail, such as MESHs, need ground-based measurements for verification and potential improvements. Drone-based photogrammetry can cover areas closer to the radar spatial resolution, which makes this approach particularly valuable for the verification of radar products.

685

690 The comparison of drone-based photogrammetry with automatic hail sensors allowed to highlight the advantages and limitations of both approaches in measuring hail (see a summary in Table 4). We here want to highlight that the clustering problem refers to many hailstones that aggregate on the ground next to each other. This predominantly occurs during hail events with dominating small hail and intense precipitation. The resulting hail clusters pose a problem to the algorithm to differentiate

695 between individual hailstones. An equivalent problem within the automatic hail sensor data is related to the dead time after
each hail impact. The dead time is necessary to avoid any interference with subsequent impacts and to perform the retrieval of
the two-stage approach from Soderholm et al. (2020) combining machine learning for detection and computer vision for size
retrieval, gives not an optimal result. The edge-detection algorithm on the pixel-lightness fails in our case for hailstones where
the edge regions show a clear ice structure and the lightness becomes similar to the background. The same problem will be
present for even simpler CV approaches without the use of neural networks, e.g. blob detection (?). If the background and
700 objects would be homogeneous enough, identifying the correct blobs and shapes is straight forward data (Kopp et al., 2023).
Furthermore, by combining data from both approaches strongly improves the reconstruction of the complete HSD and could
further extend our understanding of hailstorms.

Drone imagery acquisition Future drone-based aerial photogrammetry for hail could be improved , considering that low
light levels can be a main issue whenever the thunderstorm occurrence drags on into the night or the available light is greatly
705 reduced by the presence of the thunderstorm itself . The amount of light present in a scene governs the required exposure
time given all other camera settings are constant. The resulting exposure time essentially by having an artificial light source.
Poor light conditions are a main challenge caused by the thunderstorm itself or if the hail occurs during twilight or night. The
light conditions determine the exposure time which limits the maximum flight velocity given a sub-pixel motion blur criterion.
Adding more light in the form of a drone-mounted flash could allow to avoid any motion blur. A flash or additional light
710 source allows for an increased flight velocity while conserving the sub-pixel motion blur condition, allowing for more area
to be covered in the same time. More light would also improve image quality, as, and thus a larger area can be covered. In
addition, the image quality can be improved by reducing the sensor gain (ISO) and the aperture size could be reduced.

Nowadays, with the high availability and coverage of radar observations and sophisticated hail products, like MESHS,
the demand for objective ground truth observations of the hail size is rising to allow verification studies of the radar-based
715 algorithms. Beside crowdsourced observations, traditional hailpads and new automatic sensors, field observations with drones
can be a very useful additional information source of hail size data. The possibility to spatially collect hail size data with
drone image photogrammetry over quite large areas gives new insights into the HSD of hailstorms. Here we presented the
large discrepancies between MESHS and the hail sensor data and explain that for specific hail events the drone-based hail data
can provide additional information and thus complement automatic hail sensor measurements. Both measurement applications
720 have their advantages and drawbacks (s. Table 4). The sensor provides exact time information and is not affected by any melting
on the ground, but the limited area covered leads to truncated distributions. The drone-based approach with the large area
allows for a more representative sample of the hail size distribution, but is impacted by melting and image quality. Using those
measurement sources in combination to observe the same hail fall could improve the reconstruction of the complete HSD of
such an event and also help to frame the limitations of both applications. In this sense, it could be a good idea to carry along
725 a few traditional hailpads during storm chasing, which could be deployed right before a hail fall so that those measurements
could be compared as well with the drone-based hail data.

To further assess the hail size distribution of different storms, more observational data is crucial. However, as described in
the introduction (Sect. 1), the collection of drone-based areal photography is a time-consuming and difficult aerial photography

Table 4. ~~Schematic list of some advantages~~ Advantages (green bold font) and disadvantages (red normal font) of the two hail observation methods: Drone-based photogrammetry and automatic hail sensor. ~~With the «clustering problem» we refer to the issue, when too many hail stones are close to each other and the separation of the individual hailstones is getting difficult in the image data. On the sensor side, an equivalent problem is a dead time after each hail impact. In a worst case of fast, subsequent or simultaneous hits a separation of those is not possible.~~

	Drone-based photogrammetry	Automatic hail sensor
Sampling error	low low	high high
Melting problems	yes yes	no no
Exact time information	no no	yes yes
Probability to capture largest hailstones	high high	low low
Daylight dependence	yes yes	no no
Operational application	difficult challenging	easy reasonable
Clustering problems	high high	existing, but low existing, but low
Size estimation	direct direct	indirect indirect

of hail is a ~~time-consuming and challenging~~ task. Therefore, it could be beneficial to set up a ~~database of public database~~ of performed drone-based ~~maps for hail surveying to further adapt and test the existing algorithms~~. In addition hail surveys to enhance collaborations between different research groups on adaptation and testing of existing algorithms for various hail events. Moreover, with the increasing ~~usage~~ use of personal drones equipped with cameras, there could be a public community that ~~has brings~~ brings the basic requirements for such observations. It might ~~thus~~ be useful to provide the ~~requirements information~~ information about how to collect adequate image data and ~~use it collect such data~~ use it collect such data in a crowdsourced approach similar to the existing ~~information retrieval reporting systems~~ at weather services (e.g. ~~German Weather Service DWD and Federal Office for Meteorology and Climatology MeteoSwiss~~ or German Weather Service DWD). Another point to ~~stimulate in future could be address are~~ tests with artificial hail objects of defined size on real backgrounds such as short mowed meadows classes on different backgrounds. In this way several setups ~~can could~~ be trained, tested and optimized: Save ~~and smooth~~ drone operation in various conditions, flight missions and camera settings and precise comparison of the retrieved HSD to the known ground truth.

Data availability. The drone-based hail size data set of the 2021-06-20 event are available on request.

Author contributions. ML performed the following roles: conceptualization, methodology, software, validation, hail annotation, formal analysis, visualization, and writing the original draft. KB performed the following roles: conceptualization, methodology, storm chasing, drone operations, review and editing. AH performed the following roles: PI hail sensors, review and editing. JK performed the following roles:

745 automatic hail sensor data preparation, review and editing. SM performed the following roles: conceptualization, methodology, storm chasing, hail annotation, review and editing, and project administration. DW performed the following roles: conceptualization, methodology, hail annotation, review and editing. UG performed the following roles: initiation of hail research projects, acquisition of funding, procurement of equipment, review and editing.

Competing interests. All author declare to have no competing interests.

750 *Acknowledgements.* Hail is a severe threat to the society and on-going research is important to be able to establish risk mitigation measures. In this context, we thank the Swiss Insurance Company La Mobilière for funding the automatic hail sensors network and making the hail sensor data available for research investigations. We want to acknowledge the fruitful scientific exchange with Joshua Soderholm (Australian Bureau of Meteorology) about drone-based hail photogrammetry.

References

- 755 Allen, J. T., Giammanco, I. M., Kumjian, M. R., Jurgen Punge, H., Zhang, Q., Groenemeijer, P., Kunz, M., and Ortega, K.: Understanding Hail in the Earth System, *Reviews of Geophysics*, 58, e2019RG000 665, <https://doi.org/10.1029/2019RG000665>, 2020.
- Barras, H., Hering, A., Martynov, A., Noti, P.-A., Germann, U., and Martius, O.: Experiences with >50,000 Crowdsourced Hail Reports in Switzerland, *Bulletin of the American Meteorological Society*, 100, 1429–1440, <https://doi.org/10.1175/BAMS-D-18-0090.1>, 2019.
- Bemis, S. P., Micklethwaite, S., Turner, D., James, M. R., Akciz, S., Thiele, S. T., and Bangash, H. A.: Ground-based and UAV-Based
760 photogrammetry: A multi-scale, high-resolution mapping tool for structural geology and paleoseismology, *Journal of Structural Geology*, 69, 163–178, <https://doi.org/10.1016/j.jsg.2014.10.007>, 2014.
- Bradski, G.: The OpenCV Library, *Dr. Dobb's Journal of Software Tools*, 2000.
- Brook, J. P., Protat, A., Soderholm, J., Carlin, J. T., McGowan, H., and Warren, R. A.: HailTrack—Improving Radar-Based Hailfall Estimates by Modeling Hail Trajectories, *Journal of Applied Meteorology and Climatology*, 60, 237–254, <https://doi.org/10.1175/JAMC-D-20-0087.1>, 2021.
- [Bunkers, M. J., Klimowski, B. A., Zeitler, J. W., Thompson, R. L., and Weisman, M. L.: Predicting Supercell Motion Using a New Hodograph Technique, *Weather and Forecasting*, 15, 61–79, \[https://doi.org/10.1175/WAF-D-14-00064.1\]\(https://doi.org/https://doi.org/10.1175/1520-0434\(2000\)015<0061:PSMUAN>2.0.CO;2, 2000.</u></p><p>Chronis, T., Carey, L. D., Schultz, C. J., Schultz, E. V., Calhoun, K. M., and Goodman, S. J.: Exploring Lightning Jump Characteristics,
770 <i>Weather and Forecasting</i>, 30, 23–37, <a href=\), 2015.](#)
- Fawcett, D., Azlan, B., Hill, T. C., Kho, L. K., Bennie, J., and Anderson, K.: Unmanned aerial vehicle (UAV) derived structure-from-motion photogrammetry point clouds for oil palm (*Elaeis guineensis*) canopy segmentation and height estimation, *International Journal of Remote Sensing*, 40, 7538–7560, <https://doi.org/10.1080/01431161.2019.1591651>, 2019.
- [Feldmann, M., Hering, A., Gabella, M., and Berne, A.: Hailstorms and rainstorms versus supercells—a regional analysis of convective storm types in the Alpine region, *npj Climate and Atmospheric Science*, 6, 19, <https://doi.org/10.1038/s41612-023-00352-z>, 2023.](#)
- Fraile, R., Castro, A., and Sánchez, J.: Analysis of hailstone size distributions from a hailpad network, *Atmospheric Research*, 28, 311–326, [https://doi.org/10.1016/0169-8095\(92\)90015-3](https://doi.org/10.1016/0169-8095(92)90015-3), 1992.
- Fraile, R., Castro, A., López, L., Sánchez, J. L., and Palencia, C.: The influence of melting on hailstone size distribution, *Atmospheric Research*, 67–68, 203–213, [https://doi.org/10.1016/S0169-8095\(03\)00052-8](https://doi.org/10.1016/S0169-8095(03)00052-8), 2003.
- 780 Germann, U., Boscacci, M., Clementi, L., Gabella, M., Hering, A., Sartori, M., Sideris, I. V., and Calpini, B.: Weather Radar in Complex Orography, *Remote Sensing*, 14, <https://doi.org/10.3390/rs14030503>, 2022.
- [Goutte, C. and Gaussier, E.: A Probabilistic Interpretation of Precision, Recall and F-Score, with Implication for Evaluation, in: *Advances in Information Retrieval*, edited by Losada, D. E. and Fernández-Luna, J. M., pp. 345–359, Springer Berlin Heidelberg, Berlin, Heidelberg, 2005.](#)
- 785 Groenemeijer, P., Tuschy, H., van der Velde, O., Dahl, J., and Katzen, C.: European Storm Forecast Experiment, 2007.
- Guidi, G., Shafqat Malik, U., and Micoli, L. L.: Optimal Lateral Displacement in Automatic Close-Range Photogrammetry, *Sensors*, 20, <https://doi.org/10.3390/s20216280>, 2020.
- He, K., Zhang, X., Ren, S., and Sun, J.: Deep Residual Learning for Image Recognition, in: 2016 IEEE Conference on Computer Vision and Pattern Recognition (CVPR), pp. 770–778, <https://doi.org/10.1109/CVPR.2016.90>, 2016.

- 790 He, K., Gkioxari, G., Dollár, P., and Girshick, R.: Mask R-CNN, *IEEE Transactions on Pattern Analysis and Machine Intelligence*, 42, 386–397, <https://doi.org/10.1109/TPAMI.2018.2844175>, 2020.
- ~~Holton, J. R.: *An Introduction to Dynamic Meteorology*, International Geophysics, Elsevier Science~~
- ~~Hering, A., Morel, C., Galli, G., Sénési, S., Ambrosetti, P., and Boscacci, M.: Nowcasting thunderstorms in the Alpine region using a radar based adaptive thresholding scheme, in: *Proceedings of the 3rd European Conference on Radar in Meteorology and Hydrology*, 6, 2004.~~
- 795 Houze, R. A., Schmid, W., Fovell, R. G., and Schiesser, H.-H.: Hailstorms in Switzerland: Left Movers, Right Movers, and False Hooks, *Monthly Weather Review*, 121, 3345–3370, [https://doi.org/10.1175/1520-0493\(1993\)121<3345:HISLMR>2.0.CO;2](https://doi.org/10.1175/1520-0493(1993)121<3345:HISLMR>2.0.CO;2), 1993.
- Knight, N. C.: Hailstone Shape Factor and Its Relation to Radar Interpretation of Hail, *Journal of Climate and Applied Meteorology*, 25, 1956–1958, <http://www.jstor.org/stable/26183454>, 1986.
- Kopp, J., Schröer, K., Schwierz, C., Hering, A., Germann, U., and Martius, O.: The summer 2021 Switzerland hailstorms: weather situation, major impacts and unique observational data, *Weather*, n/a, n/a, <https://doi.org/10.1002/wea.4306>, 2022.
- 800 Kopp, J., Manzato, A., Hering, A., Germann, U., and Martius, O.: How observations from automatic hail sensors in Switzerland shed light on local hailfall duration and compare with hailpads measurements, *Atmospheric Measurement Techniques Discussions*, 2023, 1–32, <https://doi.org/10.5194/amt-2023-68>, 2023.
- Kumjian, M. R. and Lombardo, K.: A Hail Growth Trajectory Model for Exploring the Environmental Controls on Hail Size: Model Physics and Idealized Tests, *Journal of the Atmospheric Sciences*, 77, 2765–2791, <https://doi.org/10.1175/JAS-D-20-0016.1>, 2020.
- 805 Kumjian, M. R. and Ryzhkov, A. V.: Polarimetric Signatures in Supercell Thunderstorms, *Journal of Applied Meteorology and Climatology*, 47, 1940–1961, <https://doi.org/10.1175/2007JAMC1874.1>, 2008.
- la Mobilière: 2021 Annual Report in brief, Tech. rep., Mobilière Holding Ltd., Berne, 2021.
- Lin, T.-Y., Maire, M., Belongie, S., Bourdev, L., Girshick, R., Hays, J., Perona, P., Ramanan, D., Zitnick, C. L., and Dollár, P.: Microsoft COCO: Common Objects in Context, <https://doi.org/10.48550/ARXIV.1405.0312>, 2014.
- 810 ~~Lindeberg, T.: *Detecting salient blob-like image structures and their scales with a scale-space primal sketch: A method for focus-of-attention*, *International Journal of Computer Vision*, 11, 318–283, 1993.~~
- Löffler-Mang, M., Schön, D., and Landry, M.: Characteristics of a new automatic hail recorder, *Atmospheric Research*, 100, 439–446, <https://doi.org/10.1016/j.atmosres.2010.10.026>, 5th European Conference on Severe Storms, 2011.
- 815 mapillary: OpenSfM, <https://github.com/mapillary/OpenSfM>, 2020.
- ~~mapillary: OpenSfM, <https://github.com/mapillary/OpenSfM/blob/main/README.md>, 2023.~~
- ~~May, R. M., Arms, S. C., Marsh, P., Bruning, E., Leeman, J. R., Goebbert, K., Thielen, J. E., Bruick, Z. S., and Camron, M. D.: *MetPy: A Python Package for Meteorological Data*, <https://doi.org/10.5065/D6WW7G29>, 2023.~~
- Najman, L. and Schmitt, M.: Watershed of a continuous function, *Signal Processing*, 38, 99–112, [https://doi.org/10.1016/0165-1684\(94\)90059-0](https://doi.org/10.1016/0165-1684(94)90059-0), mathematical Morphology and its Applications to Signal Processing, 1994.
- 820 Nisi, L., Martius, O., Hering, A., Kunz, M., and Germann, U.: Spatial and temporal distribution of hailstorms in the Alpine region: a long-term, high resolution, radar-based analysis, *Quarterly Journal of the Royal Meteorological Society*, 142, 1590–1604, <https://doi.org/10.1002/qj.2771>, 2016.
- Nisi, L., Hering, A., Germann, U., and Martius, O.: A 15-year hail streak climatology for the Alpine region, *Quarterly Journal of the Royal Meteorological Society*, 144, 1429–1449, <https://doi.org/10.1002/qj.3286>, 2018.
- 825

- Nisi, L., Hering, A., Germann, U., Schroeer, K., Barras, H., Kunz, M., and Martius, O.: Hailstorms in the Alpine region: Diurnal cycle, 4D-characteristics, and the nowcasting potential of lightning properties, *Quarterly Journal of the Royal Meteorological Society*, 146, 4170–4194, <https://doi.org/10.1002/qj.3897>, 2020.
- OpenDroneMap: ODM - A command line toolkit to generate maps, point clouds, 3D models and DEMs from drone, balloon or kite images, <https://github.com/OpenDroneMap/ODM>, 2020.
- Pflaum, J. C. and Pruppacher, H. R.: ~~A Wind Tunnel Investigation of the Growth of Graupel Initiated from Frozen Drops, *Journal of Atmospheric Sciences*, 36, 680–689, 1979.~~
- Powers, D. M. W.: Evaluation: from precision, recall and F-measure to ROC, informedness, markedness and correlation, *CoRR*, abs/2010.16061, <https://arxiv.org/abs/2010.16061>, 2020.
- 835 [Rasmussen, R. and Pruppacher, H. R.: A Wind Tunnel and Theoretical Study of the Melting Behavior of Atmospheric Ice Particles. I: A Wind Tunnel Study of Frozen Drops of Radius < 500 \$\mu\text{m}\$, *Journal of Atmospheric Sciences*, 39, 152–158, \[https://doi.org/https://doi.org/10.1175/1520-0469\\(1982\\)039<0152:AWTATS>2.0.CO;2\]\(https://doi.org/https://doi.org/10.1175/1520-0469\(1982\)039<0152:AWTATS>2.0.CO;2\), 1982.](https://doi.org/https://doi.org/10.1175/1520-0469(1982)039<0152:AWTATS>2.0.CO;2)
- Rasmussen, R. M. and Heymsfield, A. J.: Melting and Shedding of Graupel and Hail. Part I: Model Physics, *Journal of Atmospheric Sciences*, 44, 2754–2763, [https://doi.org/10.1175/1520-0469\(1987\)044<2754:MASOGA>2.0.CO;2](https://doi.org/10.1175/1520-0469(1987)044<2754:MASOGA>2.0.CO;2), 1987.
- 840 Romppainen-Martius, O.: The Swiss Hail Network, https://www.mobiliarlab.unibe.ch/research/applied_research_on_hail_and_wind_gusts/the_swiss_hail_network/index_eng.html, 2022.
- ~~Ryzhkov, A. V., Kumjian, M. R., Ganson, S. M., and Zhang, P.: Polarimetric Radar Characteristics of Melting Hail. Part II: Practical Implications, *Journal of Applied Meteorology and Climatology*, 52, 2871–2886, 2013.~~
- [Schmidhuber, J.: Deep learning in neural networks: An overview, *Neural Networks*, 61, 85–117, <https://doi.org/https://doi.org/10.1016/j.neunet.2014.09.003>, 2015.](https://doi.org/https://doi.org/10.1016/j.neunet.2014.09.003)
- 845 Schultz, C. J., Petersen, W. A., and Carey, L. D.: Preliminary Development and Evaluation of Lightning Jump Algorithms for the Real-Time Detection of Severe Weather, *Journal of Applied Meteorology and Climatology*, 48, 2543–2563, <https://doi.org/10.1175/2009JAMC2237.1>, 2009.
- Sekachev, B., Manovich, N., Zhiltsov, M., Zhavoronkov, A., Kalinin, D., Hoff, B., TOSmanov, Kruchinin, D., Zankevich, A., DmitriySidnev, Markelov, M., Johannes222, Chenuet, M., a andre, telenachos, Melnikov, A., Kim, J., Ilouz, L., Glazov, N., Priya4607, Tehrani, R., Jeong, S., Skubriev, V., Yonekura, S., vugia truong, zliang7, lizhming, and Truong, T.: opencv/cvat: v1.1.0, <https://doi.org/10.5281/zenodo.4009388>, 2020.
- ~~Soderholm, J. S. and Kumjian, M~~
- [Shedd, L., Kumjian, M. R., Giammanco, I., Brown-Giammanco, T., and Maiden, B. R.: Automating the Analysis of Hailstone Layers, *EGUsphere*, 2022, 1–17, 2022. Hailstone Shapes, *Journal of the Atmospheric Sciences*, 78, 639–652, <https://doi.org/https://doi.org/10.1175/JAS-D-20-0250.1>, 2021.](https://doi.org/https://doi.org/10.1175/JAS-D-20-0250.1)
- 855 Soderholm, J. S., Kumjian, M. R., McCarthy, N., Maldonado, P., and Wang, M.: Quantifying hail size distributions from the sky – application of drone aerial photogrammetry, *Atmospheric Measurement Techniques*, 13, 747–754, <https://doi.org/10.5194/amt-13-747-2020>, 2020.
- SwissGeoportal: Swiss Geoportal, <https://map.geo.admin.ch/>, 2023.
- 860 Treloar, A.: Vertically integrated radar reflectivity as an indicator of hail size in the greater Sydney region of Australia, in: Preprints, 19th Conf. on Severe Local Storms, Minneapolis, MN, Amer. Meteor. Soc, pp. 48–51, 1998.
- [Van Rijsbergen, C. J.: Information retrieval. 2nd. newton, ma, 1979.](https://doi.org/https://doi.org/10.1016/j.jas.1979.05.001)

- Waldvogel, A., Federer, B., and Grimm, P.: Criteria for the Detection of Hail Cells, *Journal of Applied Meteorology and Climatology*, 18, 1521–1525, [https://doi.org/10.1175/1520-0450\(1979\)018<1521:CFTDOH>2.0.CO;2](https://doi.org/10.1175/1520-0450(1979)018<1521:CFTDOH>2.0.CO;2), 1979.
- 865 ~~World Meteorological Association: International Cloud Atlas, accessed 23 March 2023, 2017.~~
- [Wilks, D. S.: Statistical methods in the atmospheric sciences, vol. 100, Academic press, 2011.](#)
- Wu, Y., Kirillov, A., Massa, F., Lo, W.-Y., and Girshick, R.: Detectron2, <https://github.com/facebookresearch/detectron2>, 2019.
- [Wu, Y., Kirillov, A., Massa, F., Lo, W.-Y., and Girshick, R.: Detectron2, https://github.com/facebookresearch/detectron2/blob/main/detectron2/config/defaults.py, 2023.](#)
- 870 Ziegler, C. L., Ray, P. S., and Knight, N. C.: Hail Growth in an Oklahoma Multicell Storm, *Journal of Atmospheric Sciences*, 40, 1768–1791, [https://doi.org/10.1175/1520-0469\(1983\)040<1768:HGIAOM>2.0.CO;2](https://doi.org/10.1175/1520-0469(1983)040<1768:HGIAOM>2.0.CO;2), 1983.
- Zou, Z., Shi, Z., Guo, Y., and Ye, J.: Object Detection in 20 Years: A Survey, <https://doi.org/10.48550/ARXIV.1905.05055>, 2019.

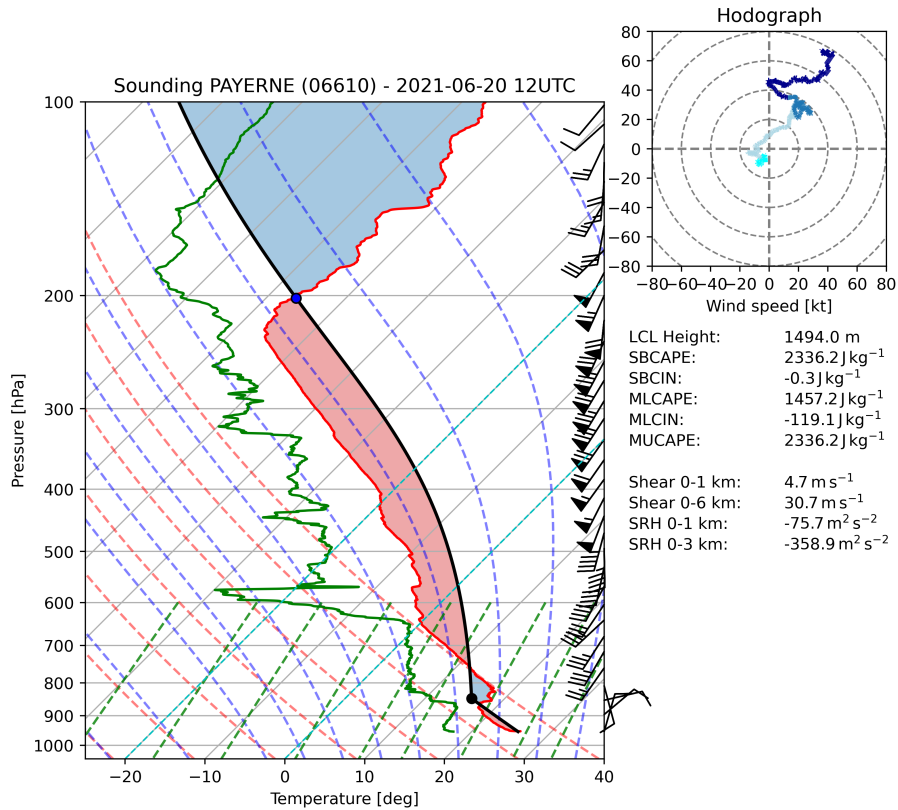


Figure 1. Skew-T plot with hodograph analysis from the atmospheric radio sounding at the Payerne station (ID: 06610, 87 km WSW from the soccer field) on 2021-06-20 12 UTC, produced with the MetPy software (May et al., 2023). The temperature and dew point profiles are drawn in red and green. The shaded areas in red and blue mark the CAPE (Convective Available Potential Energy) and CIN (Convective Inhibition). The sounding is characterized by a moist hodograph display shows four layers: 0–1 km (cyan), fairly well-mixed layer 1–3 km (light blue), separated from a dry layer above by a capping inversion. Lapse rates above the cap are close to dry-adiabatic. In meteorology this kind of sounding is also known as a «loaded gun» sounding 3–5 km (blue), 5–10 km (dark blue).

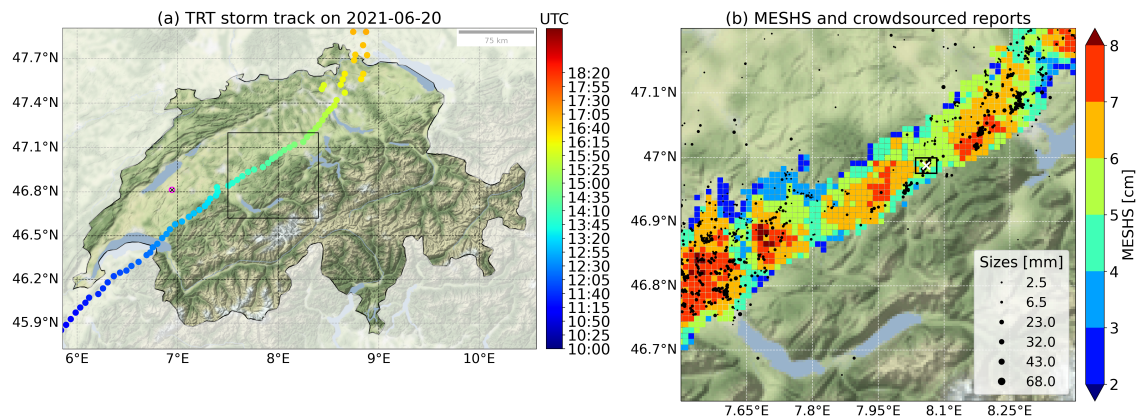


Figure 2. Storm track (a) of the 2021-06-20 supercell with colored time information (5 min resolution of the scatter points) and the location of the atmospheric radio sounding (magenta open circle with black cross inside) shown in Fig. 1. The storm location at the sounding time (12 UTC) is marked with the same edge color (magenta). The black rectangle in (a) marks the zoom area for plot (b), where information on radar derived MESHs (Maximum Expected Severe Hail Size) and crowdsourced hail size reports (black and different sized circles for 6 size categories with bin centers at 2.5, 6.5, 23, 32, 43 and 68 mm corresponding to the MeteoSwiss app categories: smaller than coffee bean, coffee bean, 1 CHF coin, 5 CHF coin and tennis ball), are given. The location of the soccer field, where the drone-based hail survey took place, is marked with a magenta cross. The white rectangle around the magenta cross in (b) marks the zoom area for the [detailed](#) map view in [Fig. 3](#).

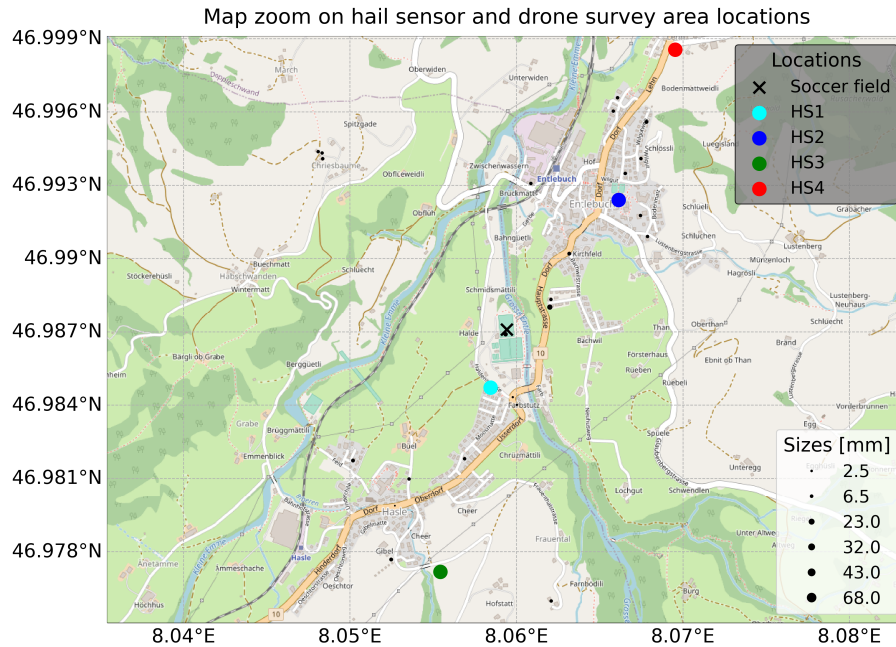


Figure 3. The zoom area and detailed view for the marked rectangle around the white cross in Fig.2(eb), where. It shows the detailed locations of the soccer field (roughly centered to the map view, magenta-black cross), the 4 nearest automatic hail sensors (HS1, HS2, HS3 and HS4) and the crowdsourced hail size data (black and different sized circles) for this area are shown. The histograms in (d) present the recorded HSDs from the automatic hail sensors together with the daily maximum MESHS value at the sensor locations. The recorded hail duration for the sensors are 3 (HS2), 52.5 (HS3) and 13 min (HS4). The HS1 sensor (cyan color) did not record any hailstones, and is thus omitted in plot (d).

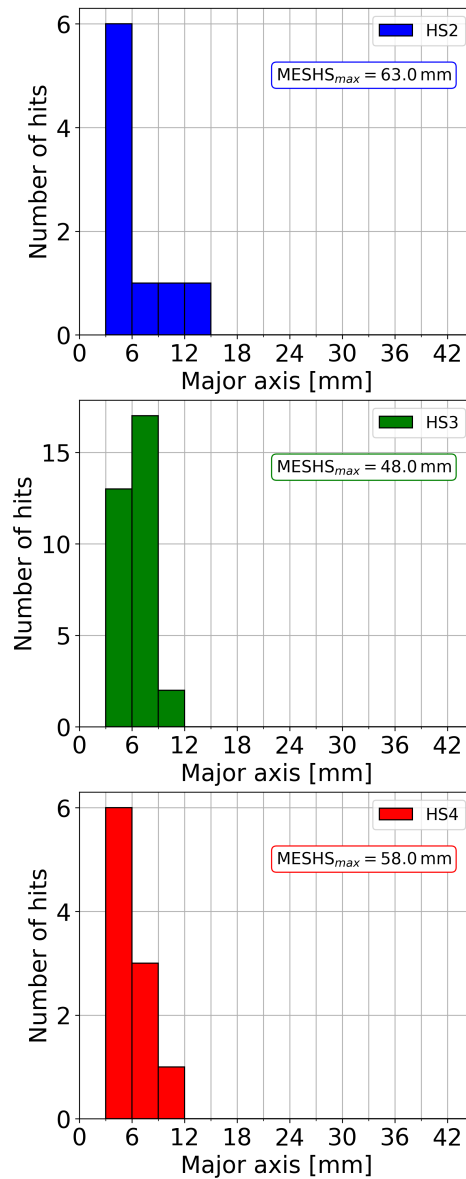
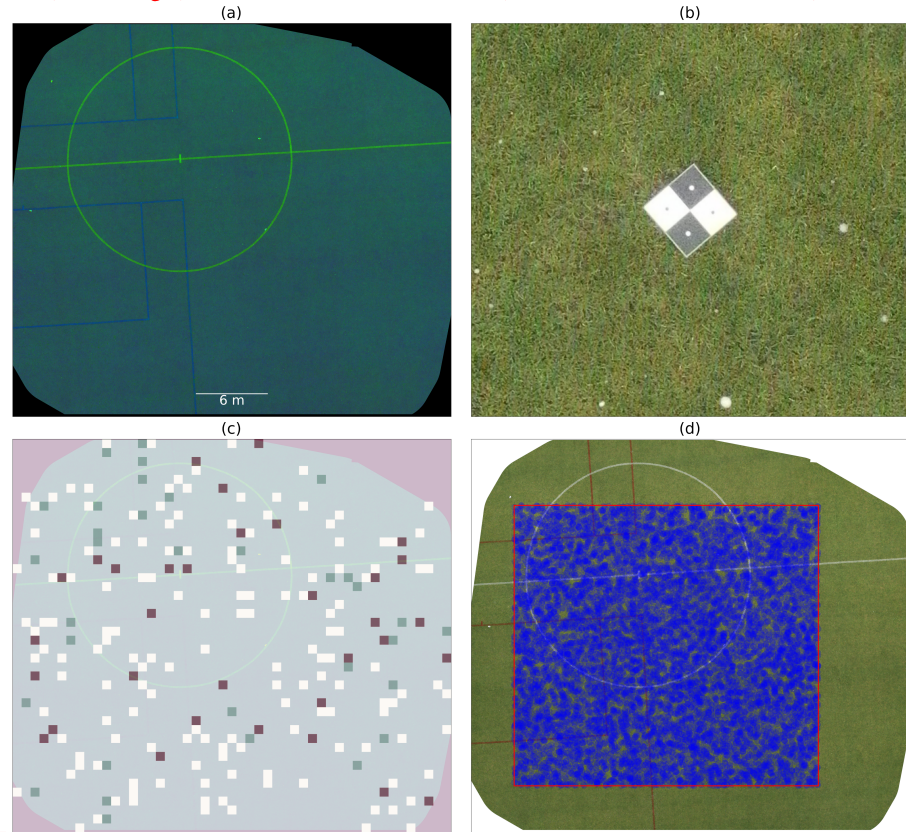


Figure 4. Histograms of the recorded hail size distributions from the automatic hail sensors together with the daily maximum MESH value at the sensor locations (see Fig. 3). The recorded hail duration for the sensors are about 3 min (HS2), 16 min (HS3) and 13 min (HS4). The color scheme follows the one from Fig. 3. The HS1 sensor did not record any hailstones, and is thus omitted here.

In (a), the final orthophoto of the 2021-06-20 hail event is shown in HSL (Hue, Saturation, Lightness) color space. It is produced from 116 individual aerial drone images with the OpenDroneMap (ODM) software package. The radius of the soccer middle circle is 9.15 m. In (b) an image zoom from the orthophoto with actual scale of 1 (width) and 0.9 (height) illustrates the hail appearance on the soccer field in conjunction with one of the reference objects (black and white circles: 10 diameters; black and white squares: 75 side lengths) to verify the ground sampling distance (GSD). In (c), the random selected distribution of training (whitish), validation (greenish) and test (reddish) image tiles (75 edge length) are displayed within the orthophoto. In (d), the same orthophoto in RGB (Red, Green and Blue) color space is shown and over-plotted by a 600 m² area (red rectangle), where 10000 circles of 0.2 m² (virtual hail sensors, blue shaded) are randomly placed for statistical assessments.



placed for statistical assessments.

Figure 5. In (a), the final orthophoto of the 2021-06-20 hail event is shown in HSL (Hue, Saturation, Lightness) color space. It is produced from 116 individual aerial drone images with the OpenDroneMap (ODM) software package. The radius of the soccer middle circle is 9.15 m. In (b) an image zoom from the orthophoto with actual scale of 1 m (width) and 0.9 m (height) illustrates the hail appearance on the soccer field in conjunction with one of the reference objects (black and white circles: 10 mm diameters; black and white squares: 75 mm side lengths) to verify the ground sampling distance (GSD). In (c), the random selected distribution of training (light grey), validation (green) and test (dark red) image tiles (75 cm edge length) are displayed within the orthophoto. In (d), the same orthophoto in RGB (Red, Green and Blue) color space is shown and over-plotted by a 600 m² area (red rectangle), where 10000 circles of 0.2 m² (virtual hail sensors, blue shaded) are randomly placed for statistical assessments.

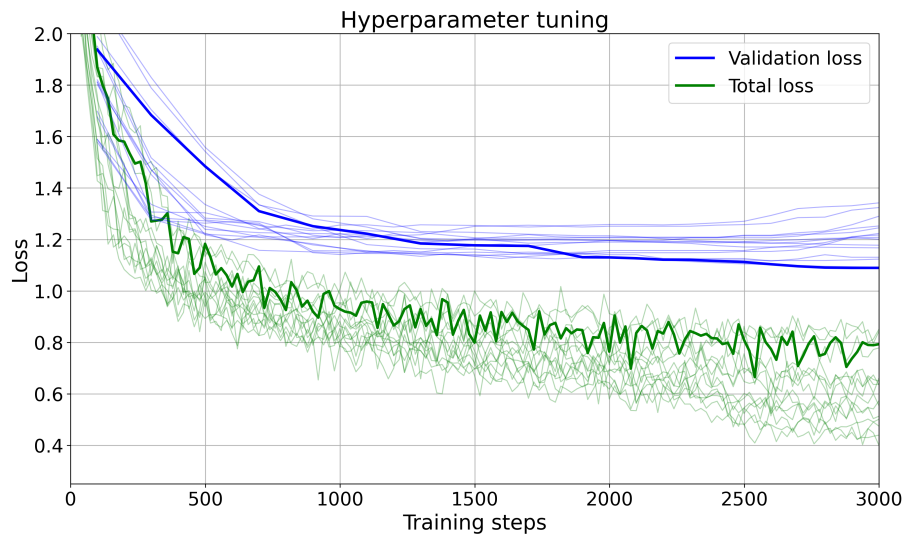


Figure 6. Spaghetti-Line plots of the evolution of validation loss and total loss along the training iteration steps for the 16 deep-learning model runs with different combinations of hyper-parameters shown in Table 1. The thick lines depict the training ~~run-3~~run-3, used for prediction of hail pixels.

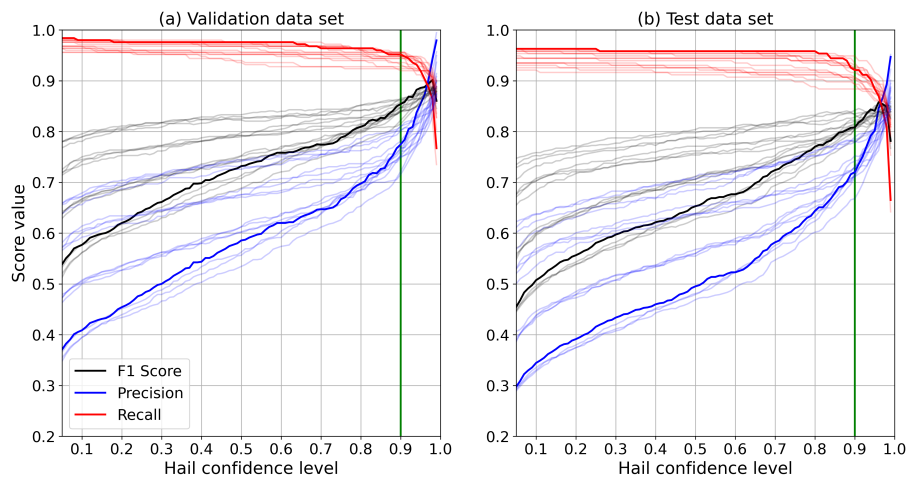


Figure 7. Spaghetti plots of precision (blue), recall (red) and $F1$ scores (black) against the hail confidence level for all 16 deep-learning model runs applied to the validation data (a) and test data (b). The thick lines depict the training ~~run-3~~run-3, used for prediction of hail pixels. The green vertical line marks the 90% hail confidence value, that has been chosen as the lower limit for the object classification.

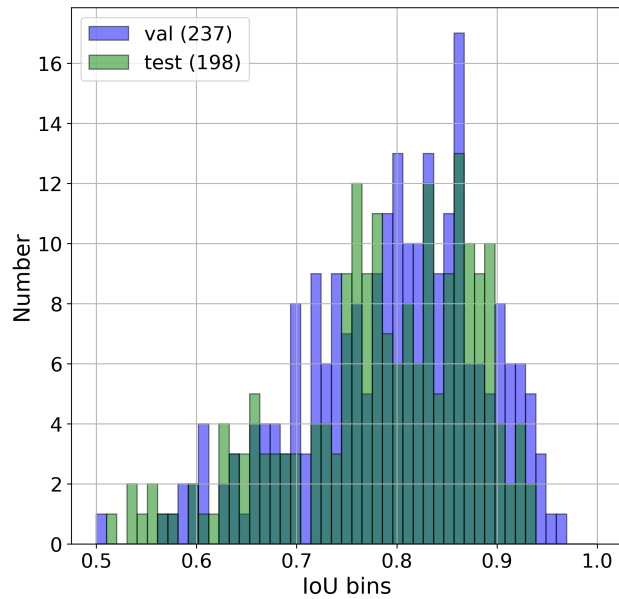


Figure 8. Histograms of IoU (Intersection over Union) ratios between model ~~run-3~~ run-3 prediction masks (hail confidence $C_i \geq 0.9$) and the validation data set (blue), respectively the test data set (green). The histogram area of the overlap between green and blue bars appears in dark green color. Only true positive (TP) matches, defined as $\text{IoU} > 0.5$, are shown. In the validation (test) data set 237 (198) hailstones are classified as TP .

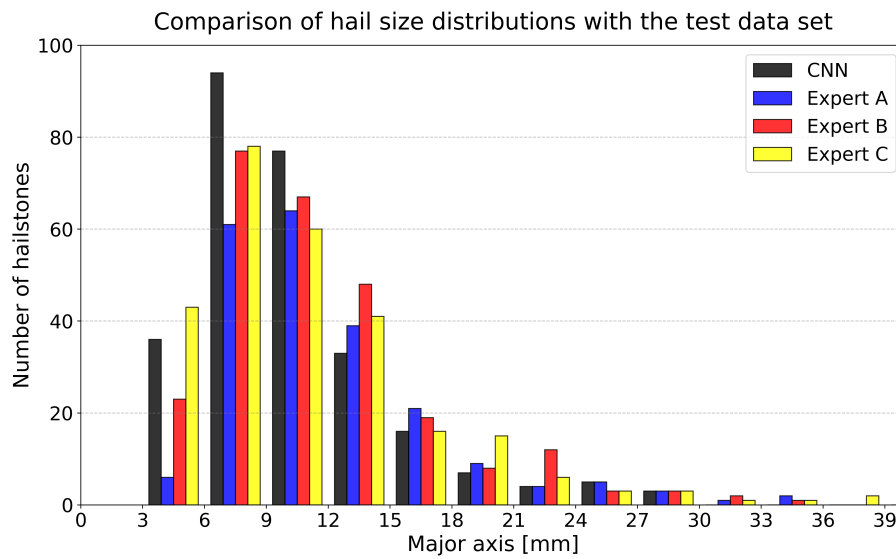


Figure 9. Comparison of four hail size distributions (HSDs) from the test data set derived from manual annotations by three experts (A: blue, B: red, C: yellow) and the prediction of the Mask R-CNN model (black). The total number of identified hailstones by the experts are 215 (A), 263 (B) and 269 (C). The CNN (Convolutional Neural Network) predicted 275 hail segmentation masks.

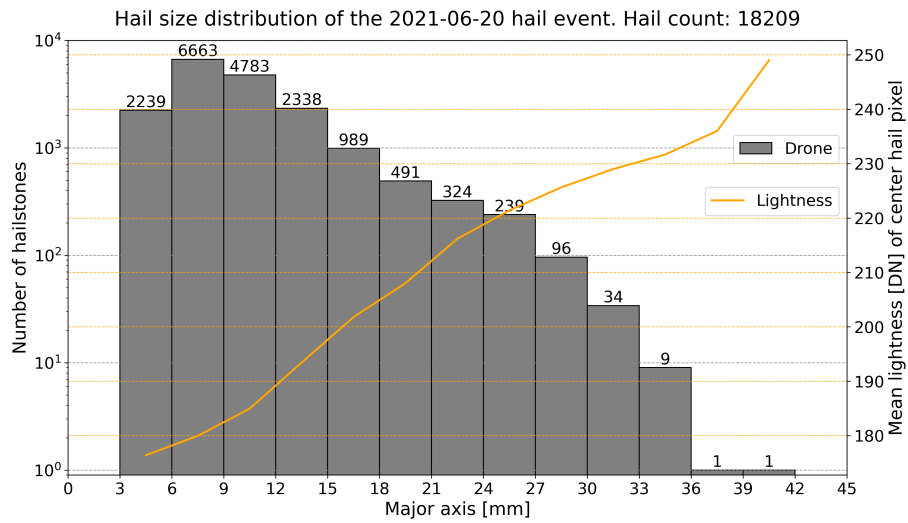


Figure 10. Logarithmic view of the time integrated hail size distribution of the 2021-06-20 event captured by the drone between 14:37:28 and 14:41:19 UTC. The total number of detected hailstones per each bin is shown with the number above each bar. All together 18209 hailstones were identified. The orange line represents the mean lightness value as digital number (DN) of all derived center hail pixels in the HSL (Hue, Saturation, Lightness) color space for each hail size bin.

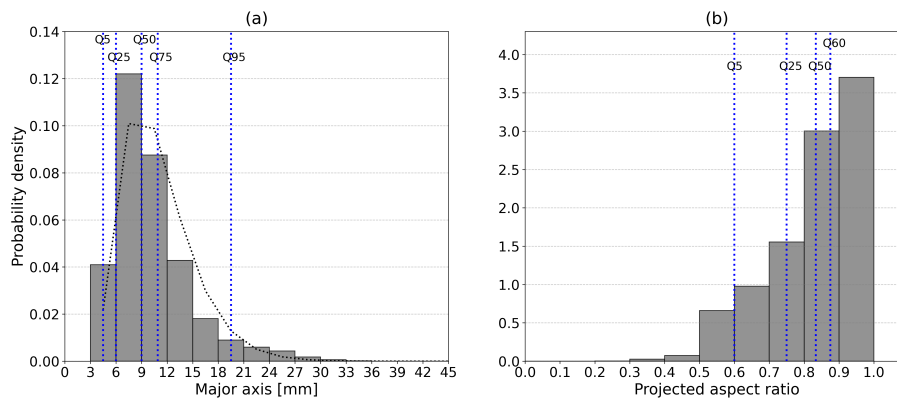


Figure 11. Probability density distributions of the hail major axis (a) and the projected aspect ratio (b) between minor and major axis length in the image plane. The vertical blue ~~and orange~~ dashed lines indicate the position of the particular ~~percentiles regarding quantiles with respect to the two X axes~~ major axis (Q5, Q25, Q50, Q75, Q95) and projected aspect ratio (Q5, Q25, Q50, Q60). The HSD in plot (a) is additionally fitted against a gamma distribution (black dotted line).

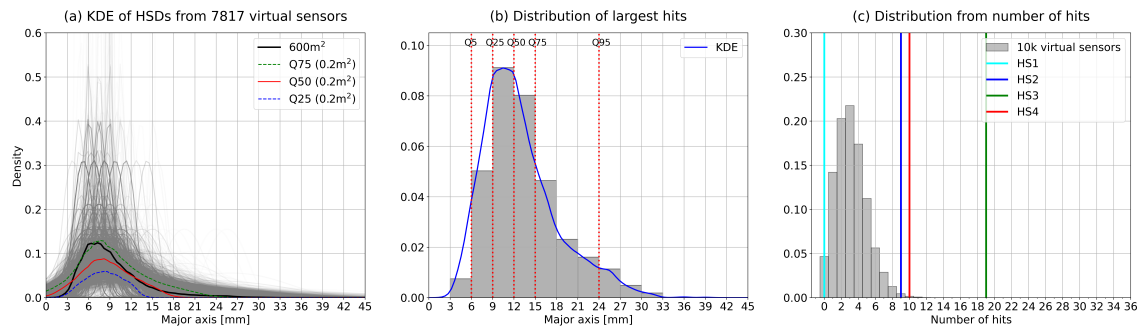


Figure 12. Kernel density estimation (KDE) of HSDs (Hail Size Distributions) from virtually and random placed simulated hail sensors at random locations (a) on an area of 600 m^2 (red rectangle in Fig. 5(d)). From the 10000 virtual HSDs 7817 can be represented by a KDE (gray curves), whereas the others do not have enough impacts. The quantiles of the sorted HSDs are shown as dashed blue (Q25), dashed green (Q75) and solid red (Q50) red-curves. For comparison, the KDE as derived from the whole 600 m^2 area is overlotted in black. In the center (b), the KDE distribution for the aggregation of the largest hailstone impact on each virtual sensor is shown. Additionally, various percentile-Quantile markers (Q5, Q25, Q50, Q75, Q95) are drawn on top of the plot (b) plot-in dashed red vertical lines. On the right side (c), the probability density for the total hits-impacts on each virtual sensor is shown as gray histogram, together with the registered number of impacts of the four closest automatic hail sensors HS1 (cyan line), HS2 (blue line), HS3 (green line) and HS4 (red line).

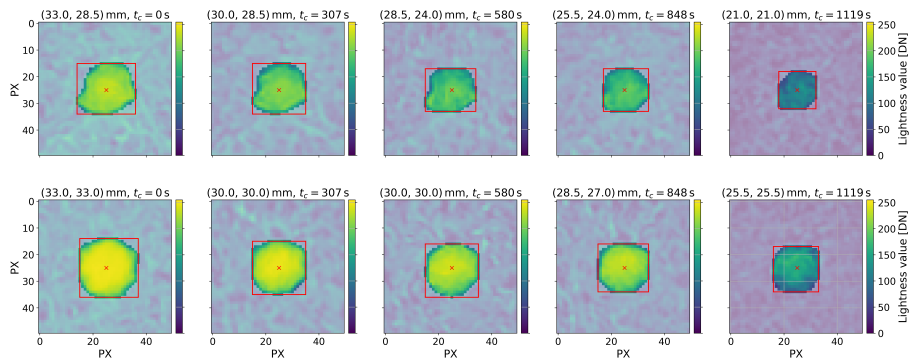


Figure 13. Two examples of hailstone size and mask shape development during the captured melting process on the ground. From left to right the sequential lightness images of two hailstones (row 1 and 2) extracted from the five orthophotos (soccer center circle) are shown. In the images the Mask R-CNN segmentation masks are emphasized together with the major and minor axis lengths indicated by the minimal bounding boxes. The actual sizes (width and height in mm) are given in the titles as well as the time t_c since first capture. During the 1119 s these hailstone-hailstones shrink about 12 mm (upper row) and 7.5 mm (lower row) in their major axis length.

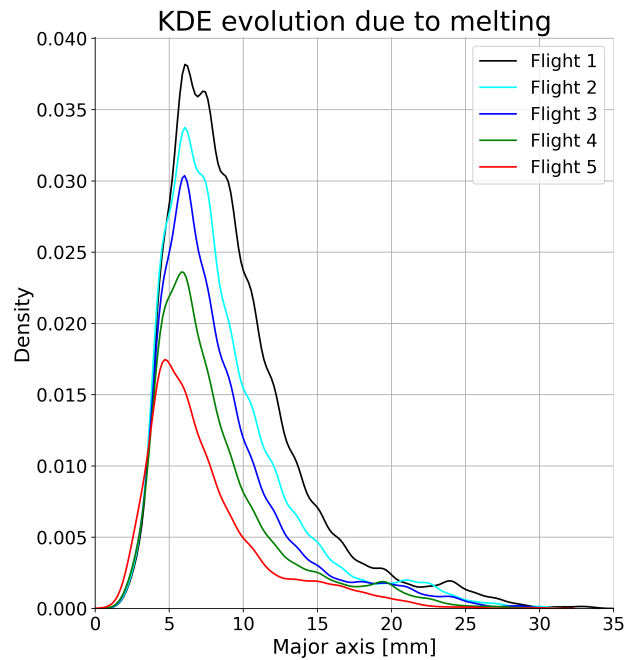


Figure 14. Kernel density estimation (KDE) with linear (a) and logarithmic (b) y-axis of the degrading hail size distributions due to melting processes on the ground. The initial hail sample size is 3925. The orthophoto area for the melting analysis is restricted to the soccer center circle to ensure a correct comparison between the different generated orthophotos (Map-Flight 1–5). In total, five drone-based hail photogrammetry surveys were carried out to secure-capture the temporal data analysis. All the relevant time frames are listed in Table 2.